Approved : _____

Timothy A. Shedd, Assistant Professor

Date : _____

Approved : _____

Gregory F. Nellis, Assistant Professor

Date : _____

The Effect of Surface Characteristics on Contact Line Motion in Immersion Lithography

by

Holly B. Burnett

A thesis submitted in partial fulfillment of
the requirements for the degree of

MASTER OF SCIENCE
(Mechanical Engineering)

UNIVERSITY OF WISCONSIN-MADISON
2005

The Effect of Surface Characteristics on Contact Line Motion in Immersion Lithography

Holly B. Burnett, M.S.
Department of Mechanical Engineering
University of Wisconsin-Madison, 2005
Professor Timothy A. Shedd, Advisor

Optical lithography has been the technology of choice in the semiconductor industry for decades. As the industry progresses, new methods are sought to manufacture smaller and faster integrated circuits. One possible next-generation lithography technology is immersion lithography. In immersion lithography, the air gap that currently exists between the last lens element of the exposure system and the wafer is filled with a liquid that more closely matches the refractive index of the lens.

There is a possibility that air bubbles, which represent a refractive index discontinuity, may be present in the liquid within the active exposure region and cause imaging errors. One potential source of bubble generation is related to the flow of liquid over previously patterned features, or topography, during scanning or filling. Another potential source of bubbles is related to droplets being deposited on the wafer surface. These droplets can re-encounter the meniscus, entraining air upon impact.

Droplets can be deposited on the wafer surface by thin film pulling or meniscus overflow. Film pulling occurs when the receding dynamic contact angle approaches 0° so that a thin film of liquid is pulled out of the meniscus. Meniscus overflow occurs when the immersion fluid does not remain contained in the gap, and instead advances with the wafer.

The contact angle is a critical parameter that governs the behavior of the contact line and therefore the entrainment of air and the deposition of droplets on the wafer surface. A hydrophobic surface is more likely to trap air than on a hydrophilic one. The contact angle can be a strong function of the flow velocity; a hydrophilic surface can exhibit hydrophobic behavior when the velocity of the free surface becomes large. Therefore, the contact angle was experimentally measured under static and dynamic conditions for a number of different surfaces, including resist-coated wafers. Contact angle hysteresis quantifies the degree of surface heterogeneity, and was also measured on these test surfaces.

The flow of liquid across surface topography was examined using both experimental visualization and CFD modeling. No air entrainment was observed or predicted over the velocity and contact angle conditions that are relevant to immersion lithography. However, experiments and CFD modeling examining droplet-meniscus impact both show that air entrainment by this mechanism is possible for immersion lithography conditions.

Receding meniscus behavior was also investigated; film pulling and meniscus overflow were observed in immersion lithography conditions. An engineering model was developed to approximately predict the critical substrate velocity leading to meniscus overflow. This model can be applied to immersion lithography system design to help avoid this behavior.

Acknowledgments

This research was supported by SEMATECH and conducted in collaboration with MIT Lincoln Laboratory and Carnegie Mellon University. Special thanks to Chris Van Peski and Andrew Grenville of SEMATECH and Intel Corporation.

To my academic advisors and supervisors, Professors Timothy A. Shedd, Gregory F. Nellis, and Roxann L. Engelstad, I extend my upmost appreciation for their continual effort, support and flexibility. Thank you to my collaborators and colleagues at the Multiphase Flow Visualization and Analysis Laboratory, the Computational Mechanics Center, and the Solar Energy Lab. I'd like to thank Adam Pautsch for his help and many clever ideas. Special thanks to Diego Aarias for his support and companionship.

This work could not have been completed without the valuable contributions of undergraduate research assistants Benjamin T. Spike and Jennifer S. Downing.

The successful completion of this project would have been insurmountable during this eventful and transitional year without the loving support of my family and friends. Thank you to Cory for providing the motivation to get this work done and the support to actually do so. Marta!!! This thesis was brought to you by cookies and beer...and of course Wisconsin cheese.

Table of Contents

List of Tables

List of Figures

Nomenclature

Symbol		Description	Units
a	=	acceleration	[m/s^2]
C	=	solution constant	
D	=	lens diameter	[m]
F	=	force	[N]
g	=	gravitational acceleration	[m/s^2]
h	=	gap height	[mm]
H	=	non-dimensional gap height	
k_1	=	optical lithography system constant	
K_v	=	viscous pressure drop factor	
L_s	=	slip length	[m]
n	=	refractive index	
NA	=	numerical aperture	
p	=	perimeter	[m]
ΔP	=	pressure drop	[Pa]
P_a	=	non-dimensional pressure gradient	
Q	=	flow rate	[m^3/s]
r	=	radius of curvature	[m]
t	=	time	[s]
T	=	total scan time	[s]
U	=	velocity	[m/s]
V_w	=	wafer velocity	[m/s]
w	=	width	[m]
W	=	line width	[m]
α	=	half of the angular aperture	[degrees]
γ	=	surface tension	[N/m]
θ	=	angle	[degrees]
λ	=	wavelength	[m]
μ	=	viscosity	[kg/m s]
ρ	=	density	[kg/m^3]
β^{-1}	=	slip coefficient	[cm^3/dyn s]

Chapter 1

Background

1.1 Immersion Lithography

Optical lithography has been the technology of choice for integrated circuit manufacture in the semiconductor industry for decades. An optical lithographic system includes an exposure tool, a mask, and a lens system. The tool is used to generate patterns on a wafer that has a light-sensitive photoresist coating on a silicon dioxide covered silicon base. An ultraviolet laser beam passes through the mask (that obstructs the light in the desired exposure pattern to create features), through the lens system, and onto the photoresist; exposure to the laser energy breaks bonds in the photoresist which shortens the polymer chains in the exposed material. After exposure, the wafer undergoes a development process that exposes the silicon dioxide beneath the developed resist but leaves the undeveloped resist. This silicon dioxide may be etched away by a number of methods. The photoresist is then removed, leaving silicon dioxide that has the pattern dictated by the features on the projection mask. At this point, the properties of the silicon substrate may be altered in the selectively exposed areas through ion implantation or other means. This process is illustrated in Fig. 1.1. The gap between the final projection lens and the wafer, subsequently referred to as the lens-to-wafer gap, is on the order of 1 mm, and the wafer is advanced under the lens system at a velocity on the order of 1 m/s. The wafer, which contains several integrated circuits, rapidly scans back and forth in order to expose each chip.

The process of applying resist, exposing, and etching is repeated several times to fabricate

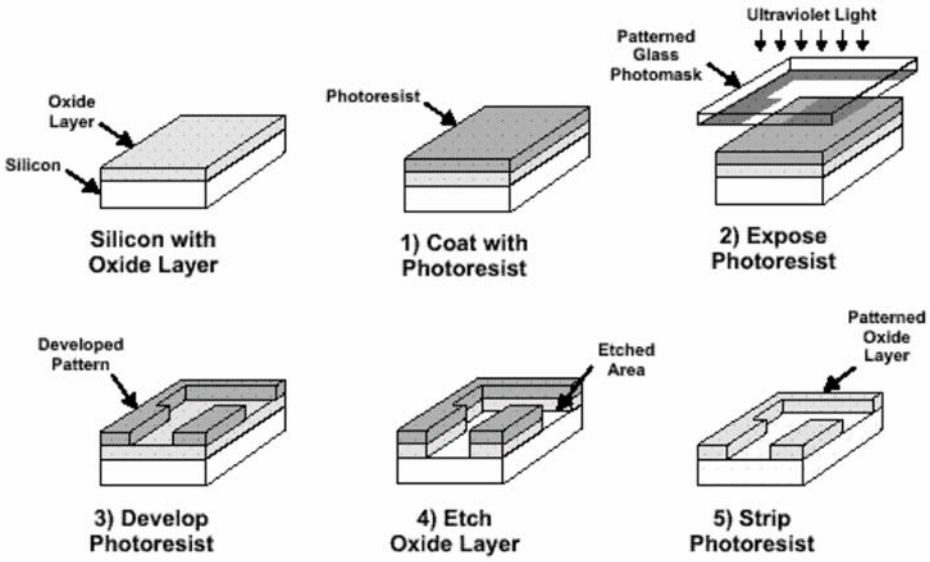

Figure 1.1: Optical lithography process overview. [Semiconductor Consulting Services, Inc., 2001]

a multilayered, three-dimensional integrated circuit. The chips are then tested and the wafer is cut up into individual integrated circuits.

As features on integrated circuits become progressively smaller, optical lithography technology is approaching its resolution limit, which is related to several parameters, including the wavelength of the illumination light. Presently, the state of the art exposure system uses a 193 nm beam obtained from an argon-fluoride excimer laser. Extending this technology to excimer lasers using fluorine with a wavelength of 157 nm is an expensive and significant proposition which will require all new optics, masks and resist materials, not all of which are production-ready [Derbyshire, 2004].

The minimum line width, W, that can be printed with optical lithography is dictated by

$$W = \frac{k_1 \lambda}{NA}, \tag{1.1}$$

where λ is the exposure wavelength, NA is the numerical aperture of the lens, and k_1 is a

constant that depends on the details of the specific exposure system. The numerical aperture of a lens is given by:

$$NA = n \sin \alpha, \tag{1.2}$$

where n is the refractive index of the medium between the lens and the substrate, and α is half of the angular aperture of the lens, as shown in Fig. 1.2.

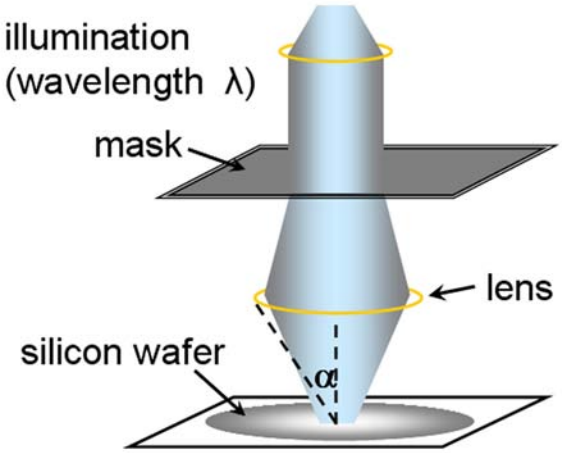

Figure 1.2: Illustration of numerical aperture.

The index of refraction for air is 1.00, yielding a maximum theoretical numerical aperture of 1 for a conventional lithography system; note that such a high numerical aperture would require an unrealistic angle (α) of 90°; a more practical maximum numerical aperture is around 0.9. The lower limit for k_1 is thought to be 0.25. A limit for minimum feature linewidth with air as a medium would therefore be around 54 nm. This is insufficient to meet 45 nm linewidths that are forecasted for 2007 [ICKnowledge, LLC, 2003].

Immersion lithography has been proposed as a potential method of extending optical lithography to smaller feature sizes. The premise behind immersion lithography is the insertion of a fluid (the immersion fluid) between the wafer and the final lens of the exposure tool, as illustrated in Fig. 1.3. The immersion fluid has an index of refraction greater than that of air. For the initial implementation of immersion lithography using 193-nm wavelength light,

the industry has selected water as the most appropriate immersion fluid. The increased index of refraction of water when compared to air allows smaller features to be printed by increasing the numerical aperture of the lens system. The depth of field performance of the system is also improved. Holding everything else constant, and using the index of refraction for ultra-pure water (approximately 1.44 [Nikon Corporation, 2004] vs. pure water which is 1.33), the minimum attainable feature using immersion lithography would be around 37 nm vs. 54 nm for a dry tool. Immersion lithography could therefore extend the lifetime of the 193-nm lithography systems by several years and delay the cost associated with moving to 157-nm lithography systems.

The implementation of immersion lithography relies on successful management of the immersion fluid. The immersion fluid must be confined to a region very near the lens and allow the wafer to scan under the lens during the exposure process. These requirements imply the existence of air/water interfaces that are bounded at the end points by advancing and receding contact lines (see the contact lines labelled in Fig. 1.3). The contact line is defined as the interface between the air, the free surface of the immersion fluid, and the wafer surface. Control of these interfaces is made more difficult by the rapid movements and accelerations of the substrate.

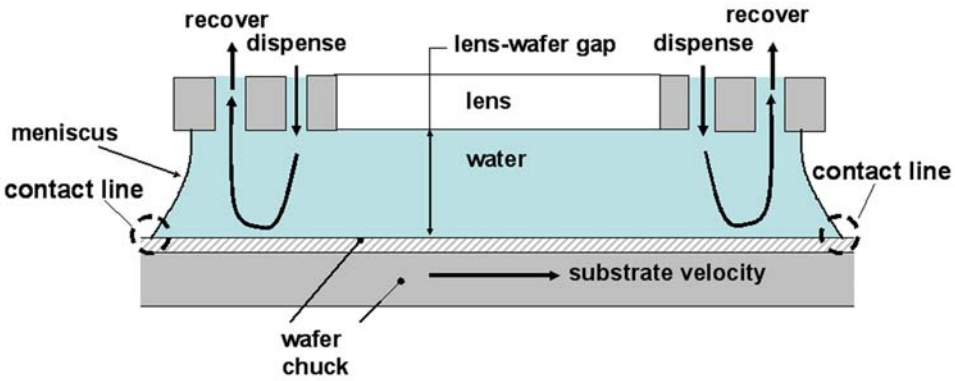

Figure 1.3: Immersion lithography relies on the insertion of a high refractive index liquid in the lens-wafer gap.

The challenges to immersion lithography include:

- photoresist-immersion fluid reactions,
- in-tool water purification system development,
- temperature-dependence of index of refraction,
- droplet deposition on the wafer surface which leads to surface contamination, and
- potential bubbles in the lens-to-wafer gap.

The focus of this work is on droplet deposition on the surface and the potential for bubbles in the lens-to-wafer gap.

1.1.1 Air Entrainment

One of the primary challenges posed by immersion lithography is the requirement that no air bubbles be present in the immersion fluid during exposure [Derbyshire, 2004]. Bubbles create an index of refraction discontinuity that will distort image patterns and therefore result in defects in the printed pattern and decreased production yield. Bubbles may originate from air entrainment at the advancing water/wafer interface or outgassing from the resist as it is exposed. Bubbles that are moving rapidly and suspended in the fluid may not significantly harm the exposure process; however, these bubbles may adhere to the wafer or lens surface in which case they are much more damaging. Recent work has indicated that outgassing from the resist does not generate problematic bubbles [Switkes et al., 2004], but there is some evidence that entrained bubbles may be an issue [Gil et al., 2004].

The relative motion between the contact line and the substrate (wafer) presents several potential mechanisms for entraining air in the fluid. These include macroscopic mechanisms such as meniscus break-up and air entrainment as the contact line folds over onto itself at

high velocity and engulfs air, as well as microscopic mechanisms such as flow over wafer topography associated with printed features [Gil et al., 2004, Wei et al., 2004]. Air entrainment is related to the dynamic contact angle, the angle that the free surface makes with respect to the substrate. The dynamic contact angle depends on the surfaces, geometry, and velocities associated with the process; when the dynamic contact angle reaches 180°, air will be entrained in the immersion fluid.

1.1.2 Liquid Deposition on Wafer

Another challenge to immersion lithography is the potential for leaving liquid behind on the wafer after it has scanned under the lens; this residual liquid may be deposited in the form of a liquid film or droplets. Residual liquid has two possible negative impacts: the fluid on the surface can evaporate and leave behind contamination, and droplets on the surface from previous scans can re-encounter the meniscus, entraining air upon impact.

A catastrophic failure of the receding meniscus that results in the deposition of large amounts of immersion fluid on the wafer has been identified and is referred to as meniscus overflow. This occurs when the immersion fluid does not remain contained in the gap, and instead advances with the wafer. Meniscus overflow results in bulk fluid loss from the lens-to-wafer gap and is aggravated by large wafer acceleration and deceleration and high wafer velocity.

A more gradual failure of the receding meniscus which results in smaller volumes of residual liquid is referred to as film pulling. Film pulling occurs when the receding dynamic contact angle approaches 0° so that a thin film of liquid is pulled out of the meniscus. Film pulling is the mechanism exploited by many coating technologies to apply a thin, uniform film of liquid to a surface.

In order for immersion lithography to succeed, it is essential that air entrainment, film

pulling, and meniscus overflow be avoided. The circumstances that lead to these failure mechanisms must therefore be characterized and understood. Each of these mechanisms is related to the behavior of the contact line.

1.2 Surface Characterization

In order to develop an understanding of the behavior of the contact line for immersion lithography, the surfaces of interest must be thoroughly characterized. This is accomplished through investigation of static contact angles, contact angle hysteresis, and dynamic contact angles on these surfaces.

Static Contact Angles

For a given liquid-solid-gas combination, the static contact angle is thought to be constant. This allows static contact angle measurement to serve as a useful surface characterization tool. The static contact angle also provides a baseline for studying the dynamic contact angle and provides input to fluid flow simulations. Static contact angle measurements are conducted on six photoresist-coated wafer surfaces and three baseline surfaces.

Advancing/Receding Angles

The static contact angle is unique on a perfect surface; however, a non-ideal surface with physical and chemical heterogeneity exhibits contact angle hysteresis. That is, as the volume of a drop on a surface is increased (by liquid addition), the contact angle will increase without contact line motion. The contact angle will eventually reach a threshold value, the advancing angle (θ_A), beyond which the contact line moves. Likewise, when the volume of the drop is reduced on an imperfect surface (by removing liquid), the droplet will exhibit a receding contact angle (θ_R) that is less than the static contact angle prior to contact line motion.

Hysteresis is defined as the difference between the advancing and receding contact angles, and provides a quantification of surface homogeneity [de Gennes et al., 2004]. Surfaces with little hysteresis are highly homogeneous, both chemically and physically. To quantify the heterogeneity of representative immersion lithography surfaces, the advancing and receding contact angles are measured.

Dynamic Contact Angles

The measurements of the static contact angles and the hysteresis provide a baseline for study of dynamic contact angles. As mentioned previously, the dynamic contact angle is critical to both air entrainment and film pulling. The dynamic contact angle also plays an important role in the meniscus instability behavior. Dynamic contact angles are measured on photoresist-coated wafers and baseline surfaces. These dynamic contact angle measurements show that the velocities associated with immersion lithography are insufficient to entrain air due to advancing dynamic contact angle alone; this observation is consistent with theory [Petrov et al., 1992]. However, the dynamic contact angle measurements indicate liquid deposition due to film pulling is possible at conditions consistent with immersion lithography.

1.3 Air Entrainment

A wafer that is in the process of being exposed is likely to have surface topography due to the features that were written during previous exposures. This topography could potentially entrain air at the contact line at lower velocities than would be expected by looking at the behavior of the dynamic contact angle. An experimental study of air entrainment due to flow over topography is conducted and the results are compared with computational fluid dynamics (CFD) simulations. The experiments and CFD simulations both indicate that air will not be entrained for the scale and shape of the surface topography that is expected in

immersion lithography.

However, an experimental study of droplets deposited on the surface re-encountering the meniscus is also presented and indicates that this process is likely to entrain air under conditions that are consistent with immersion lithography. CFD simulations of this process also indicate that air entrainment is possible.

1.4 Receding Meniscus Behavior

An engineering model for meniscus overflow, that is, bulk loss of fluid from the lens-to-wafer gap, is developed. An experimental study of the receding meniscus behavior is conducted on surfaces that represent the upper and lower bounds of immersion lithography surfaces. Parametric studies of the gap height and velocity are presented. The engineering model is capable of approximately predicting the magnitude of the critical velocity (the velocity at the onset of meniscus overflow) and can also predict how the critical velocity is affected by system design parameters. The engineering model is a valuable tool that can be used by designers to ensure that fluid deposition on the wafer surface is avoided. Both film pulling and bulk meniscus overflow are observed at velocities characteristic of immersion lithography.

Chapter 2

Surface Characterization

As the wafer moves relative to the lens and water meniscus, a thin film may be pulled from the liquid that fills the lens-to-wafer gap or droplets may be deposited onto the surface. Even with liquid cleanliness on the order of parts per billion, a single droplet evaporating on the surface of the wafer is likely to leave behind several particles that are on the order of 100 nm in size [Switkes and Rothschild, 2002]. Also, air may be entrained at the advancing meniscus resulting in free or adhered air bubbles in the exposure region that may result in imaging defects [Fan et al., 2004].

It is therefore important to characterize the geometry and operating conditions that might lead to air entrainment and film or droplet deposition. The most important facets of the system with regard to these behaviors are the interactions solid-liquid-gas interface.

2.1 Static Contact Angles

The angle made by the liquid-gas interface and the solid surface is called the static contact angle, demonstrated in Fig. 2.1. This region is sometimes referred to as the three-phase contact line or the triple line. For a static drop, the sum of the forces on the triple line must be zero. This relation is given by the Young-Dupré Law [de Gennes et al., 2004] ,

$$\gamma_{LG} \cos\theta_S = \gamma_{SG} - \gamma_{SL} \tag{2.1}$$

where γ is surface tension (N/m), the symbols L, G, and S represent liquid, gas, and solid, respectively, and θ_S is the static contact angle. The static contact angle can be measured, and the surface tension of water is known provided that the purity of the water is known. The right hand side of the equation is typically reported as a difference, as the surface energies of solid-gas and solid-liquid interfaces are not well-known.

For a given liquid-solid-gas combination, the static contact angle is thought to be constant. This allows static contact angle measurement to serve as a useful surface characterization tool. The static contact angle also provides a baseline for studying the dynamic contact angle and provides input to fluid flow simulations.

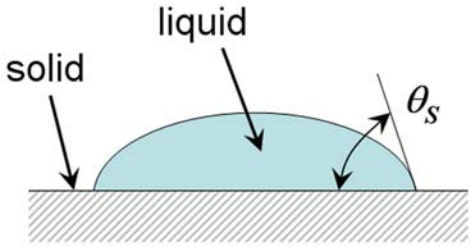

Figure 2.1: Definition of static contact angle.

2.1.1 Introduction

There are two primary techniques for experimentally measuring contact angles: the sessile drop and the Wilhelmy plate methods. The sessile drop method involves depositing a drop of liquid on a horizontal surface and observing it in cross section. The shape of the surface of the droplet, and therefore the angle that this surface makes where it meets the substrate surface, is determined optically. Commercially available systems, often called goniometers, are designed for this method, but require that an operator manually dial in a measurement and read the contact angle, introducing error of approximately $1 - 2^\circ$ [Johnson and Dettre, 1993]. More modern implementations of this technique involve imaging the drop directly

or projecting the shadow of a drop onto a screen to capture an image, then processing the digital images by computer. The Wilhelmy plate method involves the quasi-steady state raising and lowering of a thin plate into and out of a beaker of liquid. The force exerted by the fluid on the suspended plate is measured with a strain gauge, and the contact angle is calculated from the following equation [de Gennes et al., 2004],

$$F = p\ \gamma_{LG} \cos\theta_S \tag{2.2}$$

where p is the perimeter of the contact line. The sessile drop method is advantageous in that it provides a direct measurement of the angle and is relatively simple to set up. The advantages of the Wilhelmy method are that the measurement is not operator-dependent and it can be used to determine both the advancing and receding contact angles (this is discussed further in Sec. 2.2); however, this method requires test samples that are in the form of a sheet, fiber, or rod with homogeneous surface properties.

The test surfaces of concern for immersion lithography are silicon wafers that are spin-coated with a photoresist on only one side; consequently, the Wilhelmy method cannot easily be employed to investigate wafer surfaces. The sessile drop method can accommodate more varied surfaces and geometries, and its accuracy can be improved by eliminating the potential for operator error through automated image processing techniques. For these reasons, the sessile drop method was chosen for contact angle measurement of resist surfaces.

2.1.2 Experimental Setup

A schematic of the facility used to measure the static contact angle is shown in Fig. 2.2. The test surface (e.g., a resist-coated wafer) is mounted to the platform and the position of the surface can be controlled by horizontal and vertical translation stages that are affixed to a vibration-isolated optical table. An injection needle is mounted to a second vertical

translation stage so that it is perpendicular to the test surface. The dispense process is actuated by a syringe pump that is controlled via a personal computer (PC) through a LabVIEW interface. The syringe pump is used to deposit a precise volume of liquid onto the surface. Images of the droplet are acquired along an axis that is parallel to the test surface using a 1.4 megapixel, digital charge-coupled device (CCD) camera (Model QiCAM, Qimaging, Inc.) that is interfaced with, and controlled by, a PC. The camera has a resolution of 1392×1040 pixels and generates a 12-bit digital output. The entire facility is enclosed and can be purged with dry nitrogen or dry air in order to control the humidity and minimize the number of particles in the test enclosure. The humidity within the enclosure is monitored using a hygrometer. The drop is illuminated from behind by a 150-W quartz halogen fiber optic light source. A side-view image of the contact angle measurement facility is shown in Fig. 2.3.

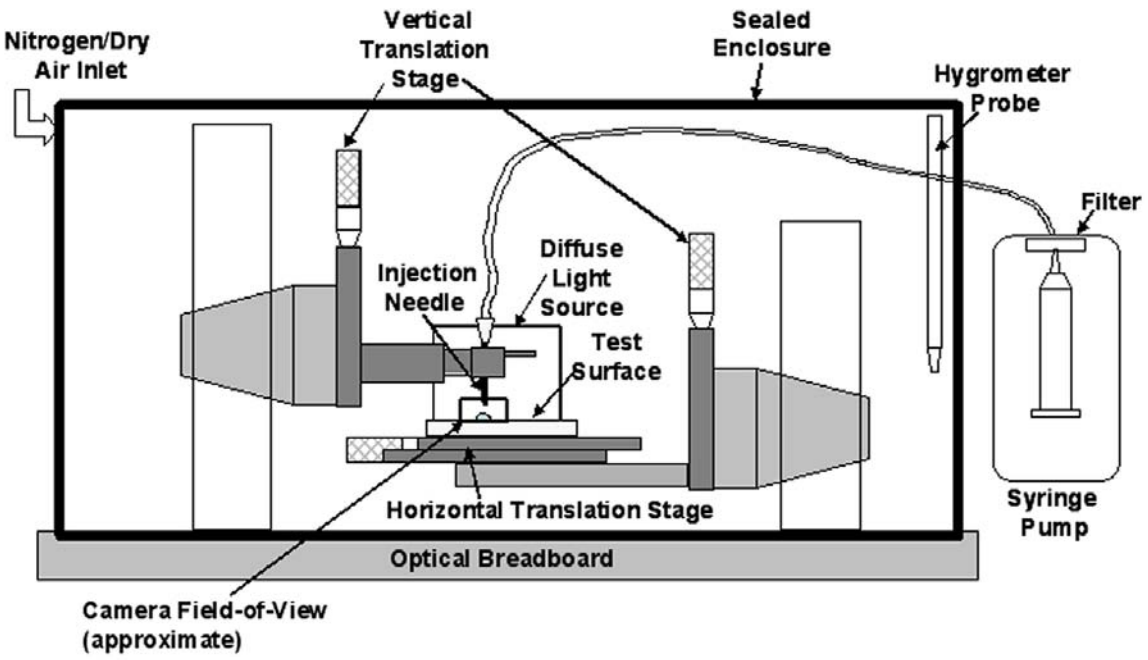

Figure 2.2: Schematic of static contact angle measurement facility.

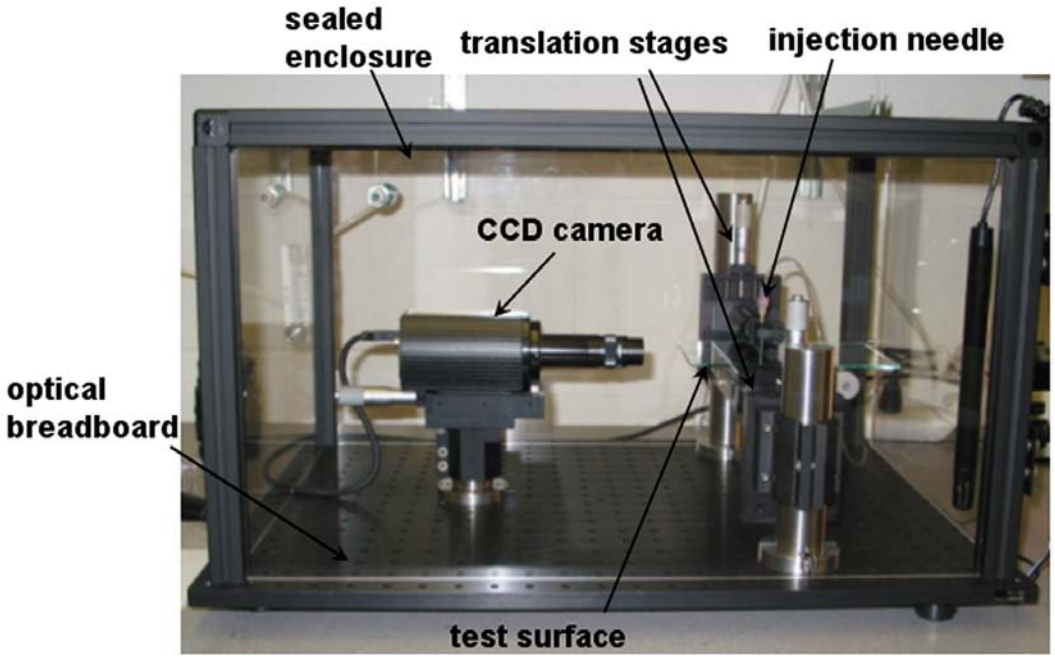

Figure 2.3: Photograph of the enclosed static contact angle measurement facility.

2.1.3 Surface Preparation

An uncoated coated test surface is prepared for contact angle measurements using the following procedure:

1. The sample is placed onto a flat, dry surface; the sample is separated from the surface by a lens tissue.

2. Any large dust particles are removed from the surface using an air canister.

3. TechSpec lens cleaner is applied to the surface. A lens tissue is lightly dropped onto the wetted surface and dragged across the surface to the edge. The lens cleaner evaporates within seconds.

4. To remove any remaining streaks, four drops of methanol are applied to a folded lens tissue and the same drop-and-drag method described in Step 3 is used.

5. The test sample is held up to a light source in order to check for any remaining streaks or particles.

A resist-coated test surface is prepared only by blowing the surface with a dry air nozzle in order to remove particulate contamination. The samples are then placed on the test platform in the enclosure.

2.1.4 Image Acquisition and Processing

By clicking the "DROP" button on the LabView interface shown in Fig. 2.4, a controlled amount of fluid (3 μl) is dispensed at a user-specified rate onto the test surface. Once the drop has been deposited on the surface, an image is acquired and stored by clicking the "SNAP" button, and the horizontal translation stage is used to move to an open location on the test sample. This process can be repeated many times in order to acquire a large batch of images for each sample.

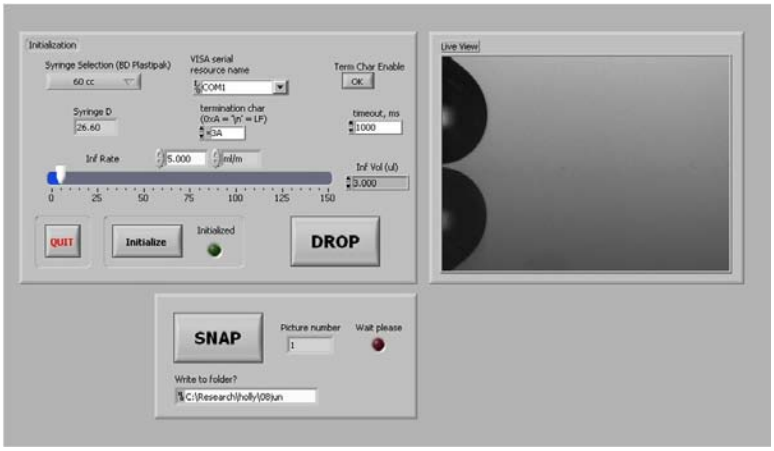

Figure 2.4: Static contact angle data acquisition LabVIEW user interface.

Once a batch of images has been acquired, it must be processed in order to determine the static contact angle. The first image of a set is acquired with a horizontal reference placed on the surface. This horizontal reference allows compensation for any alignment discrepancy

between the plane of the surface and the camera. An example of a horizontal reference image can be seen in Fig. 2.5. The image processing algorithm, written in LabVIEW, identifies a region of interest around the edge of the drop, as illustrated by the boxes shown in Fig. 2.6 for both a hydrophobic and a hydrophilic surface. Inside the region of interest, a horizontal edge finding operation is performed and the coordinates of the encountered edges are processed in order to determine the location of the contact line (i.e., the contact point where the drop meets the surface). Starting at the horizontal surface, a horizontal edge finding procedure is performed for each horizontal pixel row above the surface and repeated until 20 points along the drop edge have been identified. The angle between the horizontal reference and the line that connects the contact point and the point that lies on the edge of the droplet 20 pixels (or nominally 200 μm) from the surface is defined as the contact angle. The image processing software records the result of the calculation in a spreadsheet file and is capable of processing a large batch of images very quickly.

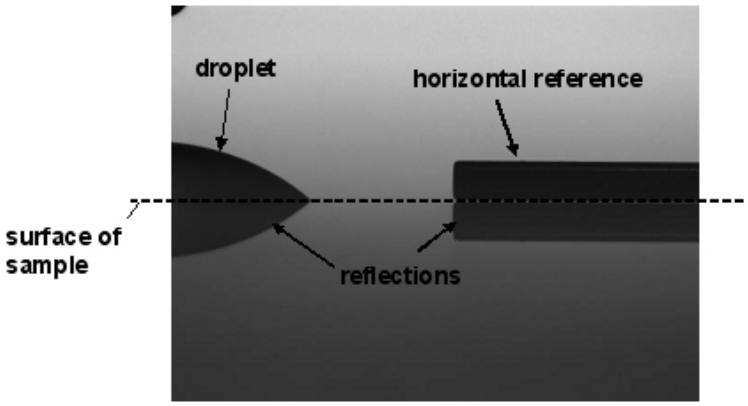

Figure 2.5: Example of an image with a horizontal reference.

The dominant sources of error related to this contact angle measurement technique are related to the ability of the image processing algorithm to locate either of the two points that are required for the contact angle calculation described above. The theoretical error due to the image processing algorithm can be examined by assuming a reasonable error in

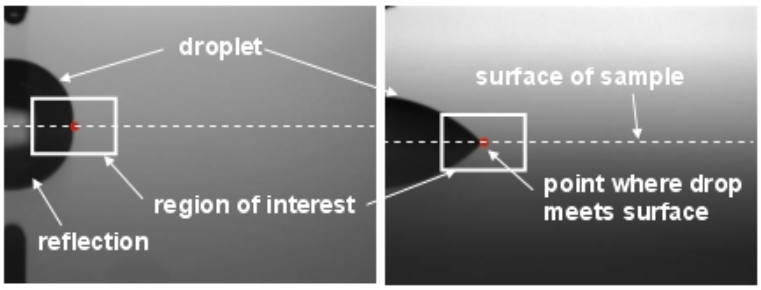

Figure 2.6: Water droplets on hydrophobic (left) and hydrophilic (right) surfaces, illustrating the region of interest identified by the image processing algorithm.

locating the position of these points (specified in terms of camera pixels). To begin with, new test points were generated by shifting either point up or down by five pixels. Using these artificially shifted points, the slope of the tangent line is recalculated and the change in the contact angle, relative to the nominally measured value, is taken to be the theoretical error. For a typical image, five pixel shifts in the location of either point will change the measurement by less than $\pm 0.6^{\circ}$; multiple image measurements will improve the uncertainty and at least 30 images are used for a typical static contact angle measurement.

2.1.5 Results

Static contact angle data were acquired on a number of test surfaces, including resist-coated wafers. The results are summarized in Table 2.1. Note that purging was unavailable for the 300 mm wafers; therefore, these measurements were made in an environment with a relative humidity of about 52%. The small standard deviation and measurement uncertainty listed in Table 2.1 shows that the system is capable of making very precise contact angle measurements. The standard deviation of the samples is always larger than the theoretical, multiple point measurement uncertainty due to surface heterogeneities (recall that each static contact angle measurement is made at a different location on the test surface). It was clear that the image-to-image deviations were in the data and not due to the measurement

Table 2.1: Static contact angle measurement results on test surfaces and wafers. Contact angles are listed with associated standard error.

Surface	Contact Angle	Standard Deviation	Number of Samples	Environment
Quartz sample from International SEMATECH	41.5° ± 0.7°	3.7°	30	17% RH (dry air purge)
Fused Silica from Edmund Optics	48.6° ± 0.9°	4.7°	30	20% RH (dry air purge)
Glass treated with Rain-X	100.6° ± 0.6°	3.1°	30	18% RH (dry air purge)
Sumitomo PAR817 (150 mm wafer)	67.7° ± 0.7°	4.4°	38	20% RH (dry air purge)
ARCH GAR8105 (150 mm wafer)	62.5° ± 0.5°	2.5°	30	22% RH (nitrogen purge)
TOK TARF7047 (150 mm wafer)	68.4° ± 0.3°	1.6°	30	21% RH (nitrogen purge)
JSR 237J (150 mm wafer)	70.0° ± 0.3°	1.6°	30	23% RH (nitrogen purge)
TOK TARF6111 (300 mm wafer)	66.8° ± 0.1°	0.8°	38	52.3% RH (no purge)
TOK TSP-3A Topcoat (300 mm wafer)	117.4° ± 0.1°	0.4°	32	52.3% RH (no purge)

technique; that is, it was obvious that the contact angle of the droplet did in fact depend on its location on the wafer and the measurement technique was accurately reporting this.

As an indication of the accuracy of this method, the measured contact angle for the 300-mm wafer coated with TOK TSP-3A topcoat treatment is $117.4° \pm 0.1°$ with a standard deviation of 0.4° (the last entry in Table 2.1). The manufacturer of the topcoat reports a 117° static contact angle measured with a commercial goniometer.

2.2 Advancing and Receding Contact Angles

On an ideal, planar, homogeneous surface, the static contact angle is unique. However, many surfaces exhibit contact angle hysteresis due to physical and/or chemical surface inhomogeneities. A drop on a flat, horizontal surface that is slowly tilted will adopt an asymmetric shape, as shown qualitatively in Fig. 2.7. The leading edge will tend to exhibit a contact angle that is greater than the horizontal static contact angle. The limiting value of this angle, that is, the value just before the drop begins to move, is defined as the advancing static contact angle, (θ_A). Similarly, the trailing edge will tend to exhibit a smaller angle than the horizontal static contact angle. The value of this angle just prior to droplet motion is defined as the receding static contact angle, (θ_R). The difference between the advancing and receding angles is referred to as the contact angle hysteresis and reflects the degree of heterogeneity of the surface as well as the effect gravity.

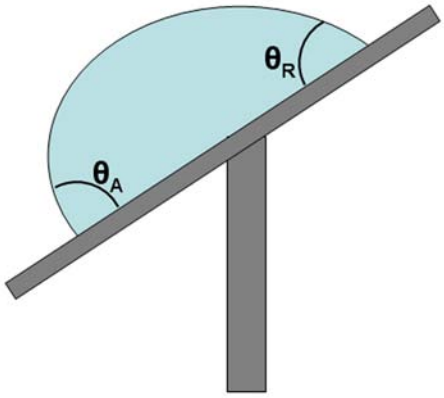

Figure 2.7: Definition of advancing and receding contact angles.

2.2.1 Experimental Setup and Procedure

To characterize the degree of contact angle hysteresis and level of homogeneity associated with a wafer surface, a tilting-plate advancing and receding contact angle measurement

facility was constructed. An image of the test facility is shown in Fig. 2.8. The facility has a test platform that can accommodate test samples up to 300 mm in diameter. This platform is mounted on a manually-controlled rotating stage. Backlighting is achieved with a 150-W quartz halogen light source directed through a hole in the center of rotating stage. A syringe pump is used to deposit a drop of deionized water through an injection needle onto the test surface in a precise location. The volume of the drops is 65 μl for wafer surfaces, 12 μl for Rain-X-treated glass, and 40 μl for all other surfaces. Precise control of drop volume ensures that gravitational effects are consistent for each surface. The operator slowly turns the rotating stage control knob, which tilts the platform and test surface. As the surface is tilted, a series of images are acquired along an axis that is parallel to the test surface using a 1.4 megapixel, digital charge-coupled device (CCD) camera (Model QiCAM, Qimaging, Inc.) that is interfaced with, and controlled by, a PC. The camera has a resolution of 1392×1040 pixels and generates a 12-bit digital output. Data images are taken using a 90 mm Nikon Mikro Nikor macro lens. The advancing and receding contact angles are measured using the image that is taken immediately before the drop begins to move. The platform tilt angle at this point is also recorded. In order to precisely characterize a surface, this process is repeated several times and a series of images is gathered and analyzed.

2.2.2 Image Processing

An example data image taken on Rain-X-treated glass is shown in Fig. 2.9. Images are processed using a custom script in IMAQ Vision Builder software. The algorithm uses an edge finding technique to locate the two contact points where the drop meets the surface, as illustrated in Fig. 2.10. A secondary edge finding operation is performed along lines that are parallel to the line defined by these two contact points in order to locate two points on the edge of the drop that are 10 pixels (200 μm) from the surface. A point 10 pixels

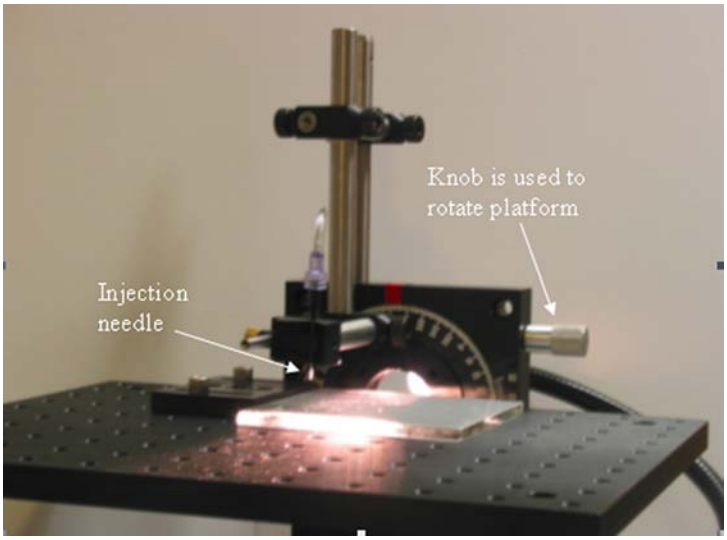

Figure 2.8: Advancing and receding contact angle measurement facility.

from the surface was selected because the drops are a smaller portion of the total image than the static contact angle measurement drops, which were processed using a point 20 pixels from the surface. These points, together with the contact points, define lines that are tangent to the drop at the advancing and receding edges. The angles between horizontal and the tangent lines are measured, as illustrated in Fig. 2.11, and the platform tilt angle is subtracted in order to determine a contact angle that matches the definition illustrated previously in Fig. 2.7. The approximate measurement error in the platform tilt angle is $\pm 0.5°$.

Figure 2.9: An example data image showing advancing and receding contact angle.

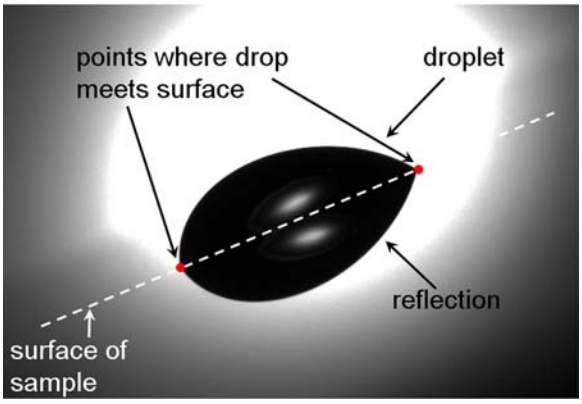

Figure 2.10: Water droplet on a wafer (TOK TARF6111), illustrating points of contact identified by the image processing algorithm.

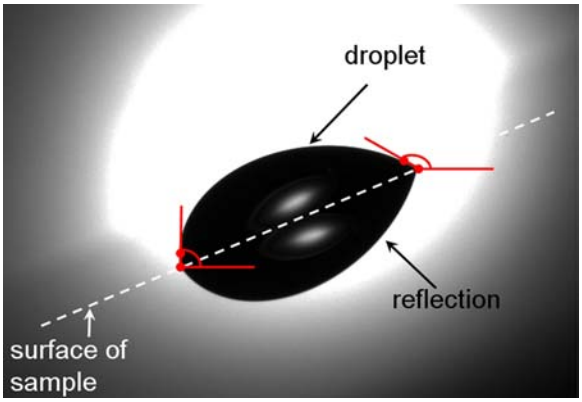

Figure 2.11: An example data image illustrating the angles identified by the image processing algorithm.

2.2.3 Results

The advancing and receding contact angle measurement results for test surfaces and six resist-coated wafers are shown in Table 2.2. The resist-coated wafers exhibit a very high degree of hysteresis. The static contact angle results presented previously (see Sec. 2.1.5) fall in between the advancing and receding contact angles for most surfaces, as expected. This was not the case for Rain-X-treated glass and the top-coated wafer; the static contact angle measured for these surfaces and reported in Table 2.1 were $100.6° \pm 0.60°$ and $117.4° \pm 0.10°$, respectively. Static contact angles for these surfaces were remeasured using the advanc-

ing/receding contact angle apparatus with no tilt, yielding $91.8° \pm 0.41°$ on Rain-X-treated glass and $107.7° \pm 0.40°$ on the top-coated wafer. These new results do fall within the measured advancing and receding contact angles for these surfaces. Recall that measurements are made on a portion of the total test sample surface area. The TOK TSP-3A top-coated wafer may exhibit regions of different static contact angle. For the Rain-X-treated surface, the difference in measured static contact angle may be due to variability in surface coating uniformity.

Table 2.2: Advancing and receding contact angle results on test surfaces and wafers. Contact angles are listed with associated standard error.

Surface	Advancing Angle	Receding Angle	Number of Images	Hysteresis
Quartz sample from International SEMATECH	50.1° ± 0.62°	34.9° ± 0.52°	30	15.2°
Fused Silica from Edmund Optics	55.8° ± 2.38°	39.5° ± 2.36°	30	16.3°
Rain-X-treated glass	94.6° ± 1.06°	87.6° ± 0.56°	24	6.9°
Sumitomo PAR817	76.8° ± 1.09°	42.6° ± 2.26°	30	34.2°
ARCH GAR8105	84.7° ± 1.28°	42.4° ± 1.44°	30	42.3°
TOK TARF7047	79.5° ± 0.42°	44.2° ± 0.50°	30	35.3°
JSR 237J	79.3° ± 0.68°	52.6° ± 0.58°	30	26.6°
TOK TARF6111	75.4° ± 0.41°	52.7° ± 0.54°	30	22.7°
TOK TSP-3A Top-coat	113.5° ± 0.33°	101.6° ± 0.45°	28	11.9°

2.3 Dynamic Contact Angles

When the contact line is in motion, the dynamic contact angle, θ_D, is different than the static advancing or receding contact angle. This contact angle difference can be thought of as being the result of a force on the fluid related to the characteristics of the flow. The force

pulling the liquid toward the dry region is given by

$$F(\theta_D) = \gamma_{SG} - \gamma_{SL} - \gamma \cos\theta_D, \tag{2.3}$$

and its effect is shown in Fig. 2.12. The dynamic contact angle can vary from 0° to 180° for a given liquid-solid-gas combination depending on the contact line velocity and the direction of its motion relative to the substrate. This variation alone can lead to the macroscopic entrainment of air at the contact line provided the contact line velocity is sufficiently large. In immersion lithography, the liquid is contained in a gap between the final lens of the exposure tool and the wafer. Voinov's equation [Petrov et al., 1992] can be used to approximately predict the effect of velocity (U, taken to be positive in the advancing case) on the dynamic contact angle,

$$\theta_D^3 = \theta_S^3 + \frac{9\mu U}{\gamma}\left[\ln\frac{h}{L_s} + C\right] \tag{2.4}$$

where h is the half-width of the gap (nominally 0.5 mm for immersion lithography), μ is the viscosity of the fluid,γ is the liquid-gas surface tension, and C is a solution constant that is equal to 1.5 for flow through a slot. In Eq. (2.4), L_s is the slip length, which is related to the inner-scale physics of the meniscus and is typically expressed as μ/β, where the slip coefficient, β^{-1}, has a value of on the order of 3×10^{-4} to 10×10^{-4} cm^3/dyn s [Petrov et al., 1992]. The exact value of the slip length has a very small effect on the dynamic contact angle. Note that Voinov's equation is strictly valid for vanishingly small Reynolds number flows, whereas the flow conditions expected in immersion lithography will be characterized by a relatively large Reynolds number, on the order of 1000. Nevertheless, the correlation provides some understanding regarding the likely impact of substrate motion on the behavior of the meniscus.

The macroscopic phenomenon referred to as air entrainment on a flat surface occurs when

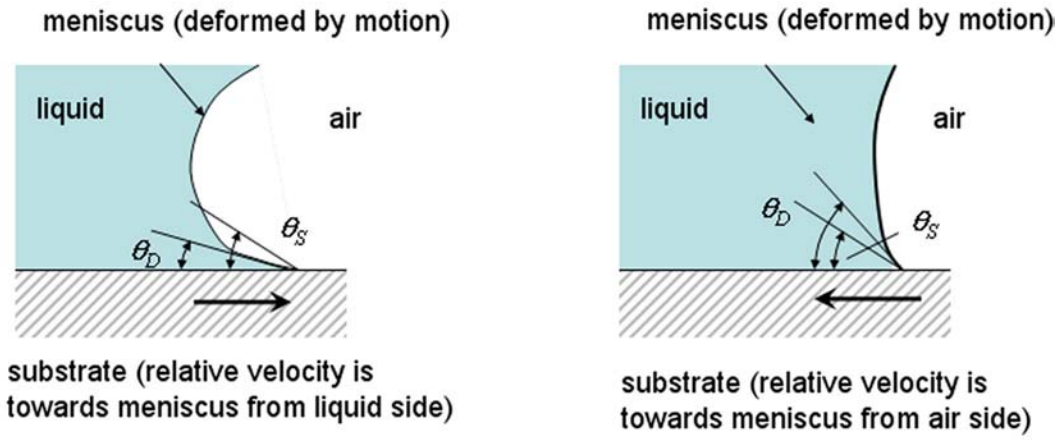

Figure 2.12: A non-equilibrium force exerted on the triple line results in dynamic contact angles.

the substrate moves into the meniscus (towards the liquid side, see Fig. 2.12) with sufficient velocity so that the dynamic contact angle approaches 180°, at which time air is pulled into the liquid at the substrate surface. Equation (2.4) indicates that for surfaces with static contact angles ranging from 60° to 120°, the velocity required to produce macroscopic air entrainment of this nature with water exceeds 17 m/s, which is well above the expected substrate velocity for immersion lithography. However, since the flows anticipated in immersion lithography do not exhibit vanishingly small Reynolds numbers, experimental investigation is required to confirm that air is not entrained at the relevant velocities.

2.3.1 Initial Dynamic Contact Angle Measurements

Experimental Setup

In order to measure the dynamic contact angle, the static contact angle facility described in Sec. 2.1.2 was initially modified as shown in Fig. 2.13. The injection needle is mounted parallel to the surface of interest and used to dispense fluid with a controlled flow rate in a stream of fluid that travels across the surface. Note that the liquid is not contained in a gap in this setup. A complementary metal oxide semiconductor (CMOS) high speed camera

(Model XS-3 Industrial, IDT, Inc.) is used to acquire a series of images as fluid is injected over the surface. The camera has a resolution of 1280×1024 pixels and generates a 10-bit digital output. The frame rate at full resolution is 628 frames per second (fps), and frame rates of up to 32000 fps can be achieved by setting a smaller region of interest. The velocity of the contact line is measured directly by displacement between successive images rather than inferred from the rate of fluid injection.

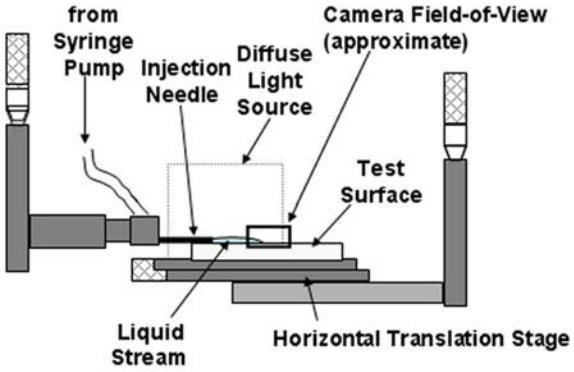

Figure 2.13: Dynamic contact angle measurement facility, as seen from the point of view of the camera.

Image Processing

Dynamic contact angle measurements make use of the same image-processing algorithm that is described in Sec. 2.1.4. However, in addition to the contact angle measurement, the velocity of the contact line is determined from the images by calculating the change in the horizontal position of the contact point between consecutive frames. Examples of dynamic contact angle images can be seen in Fig. 2.14 . With this setup, fewer images can be collected for a dynamic contact angle measurement due to the compromise between resolution and field-of-view.

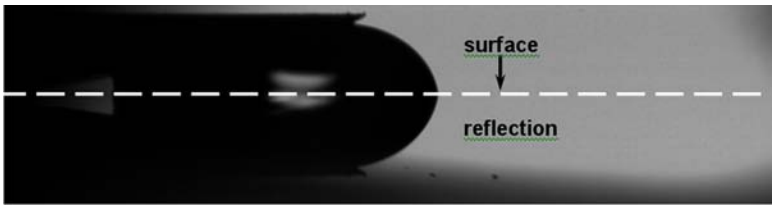

Figure 2.14: Sample of a dynamic contact angle data image. Surface is ARCH GAR8105, velocity is 0.022 m/s, and the dynamic contact angle is 79° with a standard deviation of 0.79° over three images.

Results

Dynamic contact angle measurements for the six resist-coated wafers that are listed in Table 2.1 were made at three velocities; these measurements are summarized in Table 2.3. The contact angle exhibits a clear jump at almost zero velocity which represents contact angle hysteresis. The trend with velocity is less clear and requires further investigation. The contact angle measurement technique is identical to that of static contact angles, which was validated previously. However, for these initial measurements, the fluid structure is not well-controlled and the fluid is simultaneously accelerating and spreading. The top surface of the liquid is unconstrained leading to non-uniform liquid thickness and bulging near the advancing contact line. These phenomena may lead to changes in the contact angle that are independent of the velocity.

2.3.2 Dynamic Contact Angle Measurements with Modified Setup

In order to address the shortcomings of the initial dynamic contact angle measurements, an improved fluid management system was constructed and implemented with a motorized stage in order to obtain a more controlled fluid flow condition and also allow the investigation of higher contact line velocities.

Table 2.3: Dynamic contact angle preliminary study results on resist-coated wafer surfaces.

Surface	Environment	Static Contact Angle	Velocity	Dynamic Contact Angle	Standard Deviation	Number of Images
Sumitomo PAR817 (150 mm wafer)	20% RH (dry air purge)	67.7° ± 0.7°	44 mm/s	91.7°	3.2	10
			125 mm/s	86.2°	2.8	6
			187 mm/s	97.2°	1.5	7
ARCH GAR8105 (150 mm wafer)	22% RH (nitrogen purge)	62.5° ± 0.5°	55 mm/s	77.2°	3.1	5
			110 mm/s	81.0°	0.8	8
			143 mm/s	75.5°	1.5	6
TOK TARF7047 (150 mm wafer)	21% RH (nitrogen purge)	68.4° ± 0.3°	66 mm/s	89.4°	0.2	3
			88 mm/s	99.9°	1.1	12
			176 mm/s	81.5°	0.8	7
JSR 237J (150 mm wafer)	23% RH (nitrogen purge)	70.0° ± 0.3°	55 mm/s	87.4°	2.4	8
			121 mm/s	80.8°	1.7	7
			176 mm/s	79.9°	2.4	6
TOK TARF6111 (300 mm wafer)	52.3% RH (no purge)	66.8° ± 0.1°	77 mm/s	85.6°	3.5	7
			110 mm/s	84.7°	4.9	10
			154 mm/s	84.8°	3.2	8
TOK TSP-3A Topcoat (300 mm wafer)	52.3% RH (no purge)	117.4° ± 0.1°	66 mm/s	115.4°	2.5	11
			110 mm/s	116.5°	1.5	8
			182 mm/s	119.3°	0.7	6

Experimental Setup

In order to observe dynamic contact angles under quasi-steady flow conditions, it was necessary to build a test facility with a nominally stationary meniscus that could be imaged continuously as a substrate advanced into it. Such a facility is shown in Fig. 2.15. Distilled water is injected manually into a gap between a 1-inch diameter window suspended above the substrate. The gap height can be precisely set using a digital micrometer. The substrate is mounted to a motorized linear stage, and the stage velocity is controlled via a computer interface. The substrate is then advanced into the meniscus and a series of side-view images of the meniscus are taken with the high-speed camera. Lighting is achieved with two 150-W quartz-halogen fiber optic light sources. One is used to illuminate the meniscus from the

front, while the other is aimed at a reflective surface behind the meniscus, providing back-lighting. The frame rate required increased from 100 Hz to 2000 Hz and the shutter speed required decreased from 0.5 ms to 0.05 ms as the substrate velocity was increased from 0.01 m/s to 1.0 m/s. As the substrate velocity increases, the frame rate was increased in order to acquire a sufficient data set in the time associated with the limited travel of the motorized linear stage. Blurring will occur at these higher velocities if a short shutter speed is not used. The camera settings for the dynamic contact angle image acquisition included a 10-bit pixel depth and a sensor gain of four. These settings enabled useful data to be extracted from images with minimal light and high shutter speeds. This test facility allows acquisition of large data sets, as the meniscus remains in the field of view of the camera at all times.

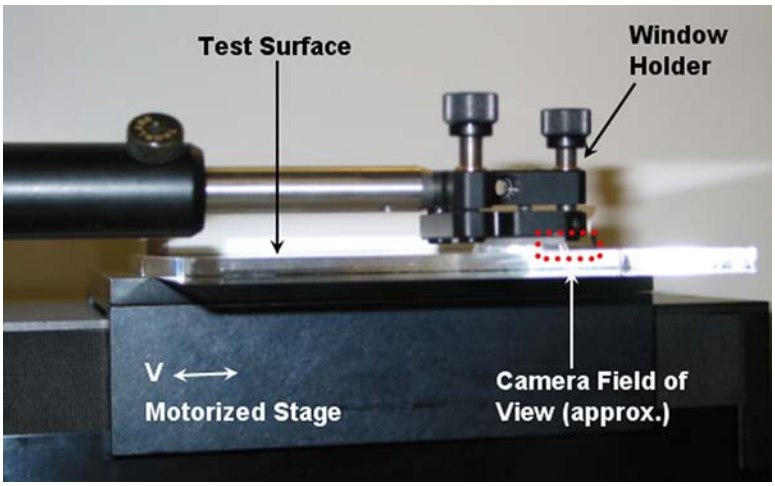

Figure 2.15: Image of the modified dynamic contact angle measurement facility.

Image Processing

An example of a dynamic contact angle data image is shown in Fig. 2.16. The sets of images are batch processed using IMAQ Vision Builder software. The image contrast is enhanced by multiplying each pixel value by a constant, ranging from 3 to 12, depending on the brightness of the image (darker images require a higher multiplier). The edge finding tool

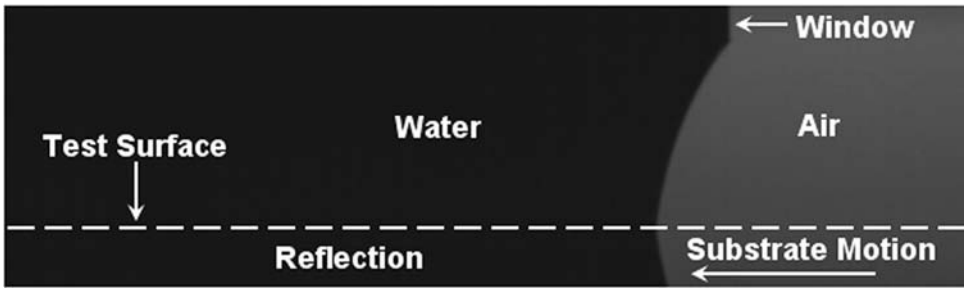

Figure 2.16: Example of a dynamic contact angle data image, taken on wafer with surface TOK TARF7047 at 0.05 m/s.

is then employed to determine the line that is tangent to the meniscus at the point where it meets the surface. The tangent line is defined in a manner that is consistent with both the static contact angle and contact angle hysteresis measurements. The dynamic contact angle is defined as the angle between the substrate surface and the line drawn between the contact point and the point on the meniscus edge 10 pixels above the surface. Batches of images are processed automatically and the resulting angles are written directly to an Excel spreadsheet. As the substrate moves into the meniscus at higher velocities, the meniscus may go out of focus due to distortions of the contact line and the images become progressively darker due to the faster shutter speeds. Any data images that are out of focus are rejected. The image multiplier and the contrast settings of the edge finding tool must be adjusted according to image brightness. A digital image processing local averaging filter is sometimes employed to improve contrast for darker images. A 3×3 local averaging filter creates a new image by determining each pixel value from an average of the adjacent pixel values in the original image. This also acts to blur any blemishes that might be exaggerated by the multiplier.

Results and Discussion

To select an appropriate gap height for conducting a series of dynamic contact angle experiments, a preliminary study on the effect of gap height was conducted using a quartz

substrate. The gap height was varied and the dynamic contact angle was measured at three velocities. The results of this study are depicted in Fig. 2.17. For gap heights of 1 mm and smaller, changes in gap height have a minor effect, if any, on the measured dynamic contact angle. At gap heights greater than 1 mm, the contact angle tends to decrease somewhat with increasing gap height. For ease of imaging, the largest possible gap height is ideal, as it allows the most light. As a compromise, a gap height of 1 mm was selected for further experimentation.

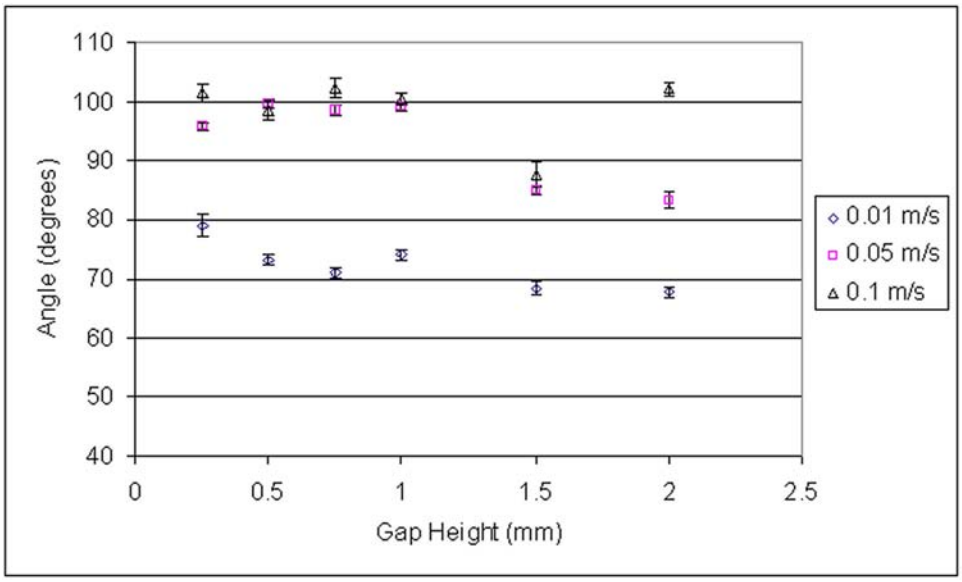

Figure 2.17: Dynamic contact angle versus gap height on quartz substrate at three velocities. (See Appendix for data.)

Dynamic contact angles were measured on quartz and Rain-X-treated glass at a gap height of 1 mm and velocities ranging from 0.01 to 1 m/s. The results are shown in Fig. 2.18. For the range of velocities investigated, the quartz exhibits a large increase in contact angle with increasing velocity from 0.01 m/s to 0.1 m/s and then increases slightly as the velocity increases beyond that point. The dynamic contact angle on the Rain-X-treated glass increases slightly as velocity increases over the entire velocity range, from 0.01 m/s to 1 m/s.

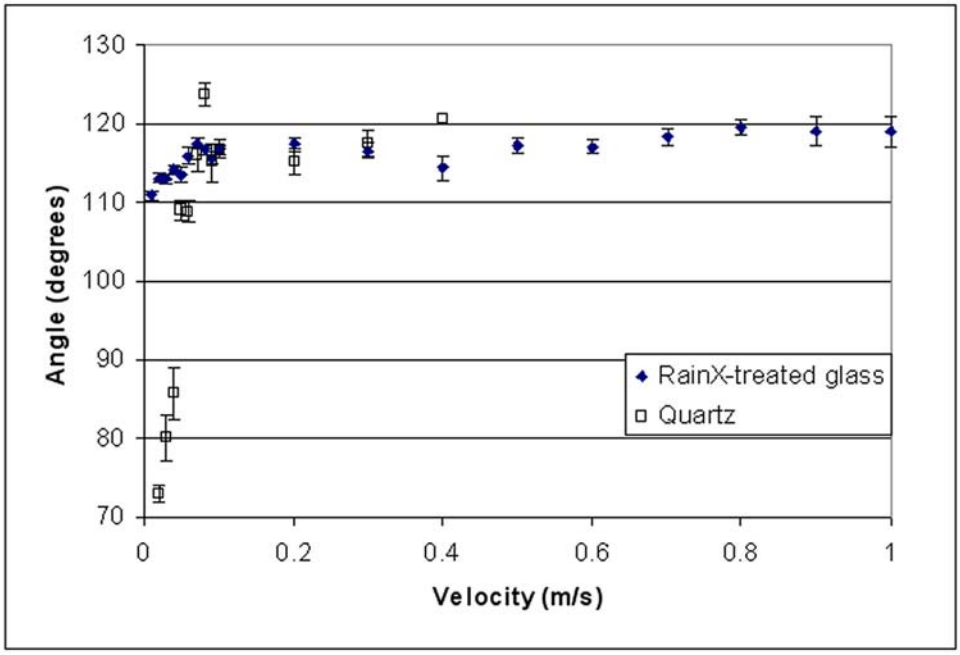

Figure 2.18: Dynamic contact angle results for Rain-X-treated glass and quartz substrates. Shown with 95% confidence interval bars. (See Appendix for data.)

Figure 2.19 shows dynamic contact angle results and corresponding 95% confidence intervals on resist-coated wafers for velocities ranging from 0.01 to 0.1 m/s. Generally, the dynamic contact angle increases slightly with increased velocity over this velocity range. Surface ARCH GAR8105 is the one exception to this; it exhibits a minor decrease in dynamic contact angle as the velocity is increased. The dynamic contact angle on the wafer surface TOK TARF6111 shows the greatest sensitivity to velocity, and the top-coated wafer TOK TSP-3A shows the least change over this range. Note that TOK TARF6111 is the surface with the largest standard deviation in the dynamic contact angle measurement while TOK TSP-3A is the surface with the smallest standard deviation. The standard deviation in the measurement is related to the degree of surface heterogeneity. Recall from 2.1.5 that the top-coated wafer is the most homogeneous of the tested resist-coated surfaces.

Dynamic contact angle results for velocities ranging from 0.1 to 1.0 m/s are shown in Fig. 2.20. There is greater scatter in this velocity range, however, the same trend holds

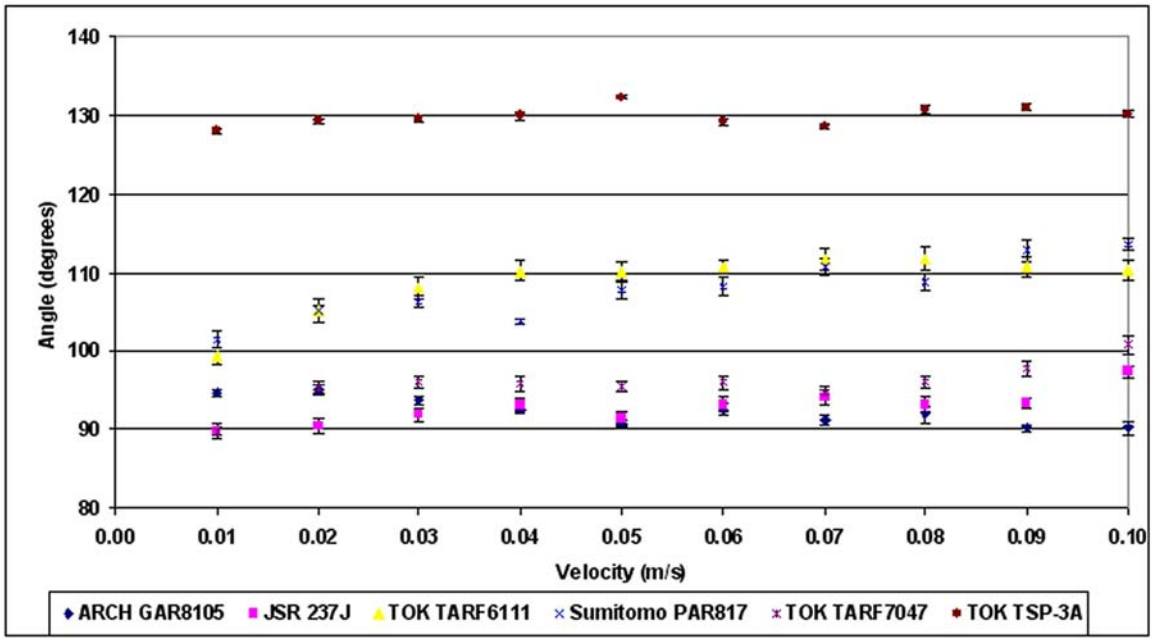

Figure 2.19: Dynamic contact angle results on wafer surfaces for velocities from 0-0.1 m/s. Shown with 95% confidence interval bars. (See Appendix for data.)

true: the dynamic contact angle tends to increase with increasing velocity. However, as the velocity increases, eventually each of these surfaces achieves a flow condition at which the liquid becomes unstable and does not remain in the gap; instead it advances with the surface and is pulled out of the gap entirely. (A detailed discussion of this behavior is presented in Chapter 4.) For this reason, data cannot be taken on every surface up to the maximum stage velocity of 1.0 m/s. As the velocity increases and this fluid instability is approached, some data are taken where the fluid and the substrate are both in motion, but at different velocities; Fig. 2.21 illustrates images where this is true (note that the window edge is chamfered). The highest-velocity data point for a substrate may deviate from the trend of dynamic contact angle increasing with velocity due to this effect.

Two distinct contact angles were observed on the surface Sumitomo PAR817, as seen in Fig. 2.22. The same behavior was observed on the JSR237J surface, but to a lesser extent. The transition from one angle to the other occurs consistently at the same location on the

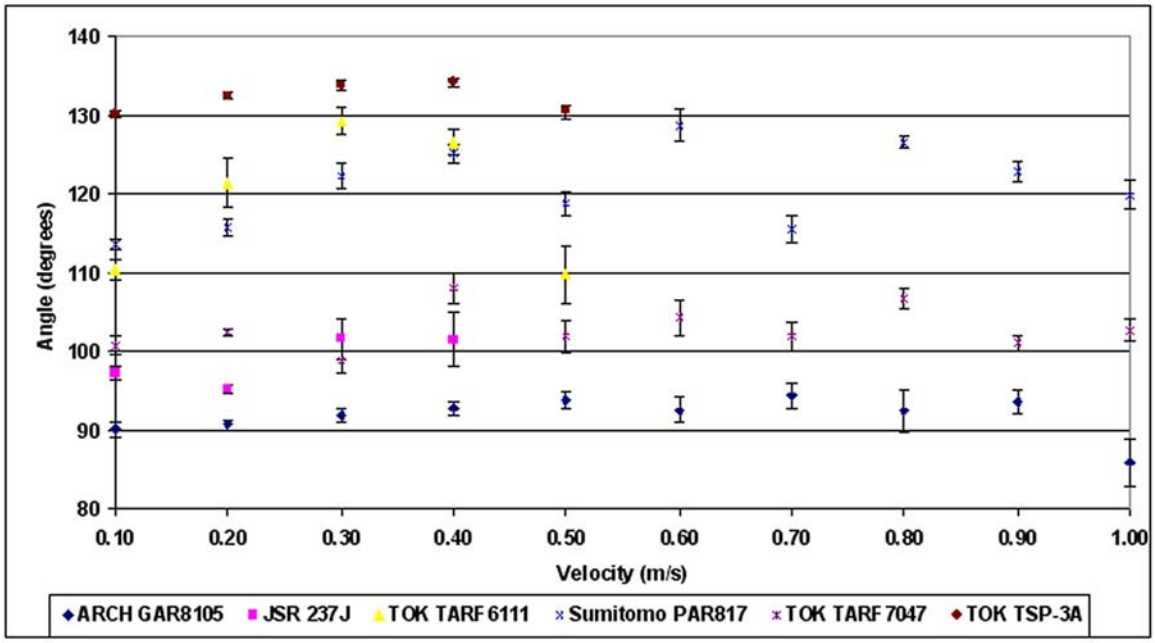

Figure 2.20: Dynamic contact angle results on wafer surfaces for velocities from 0.1-1.0 m/s. Shown with 95% confidence interval bars. (See Appendix for data.)

surface, revealing a transition in the surface topography or chemistry. The tested area of each wafer is a small percentage of the total wafer area. These types of inhomogeneities may also be present on the untested areas of the other wafers.

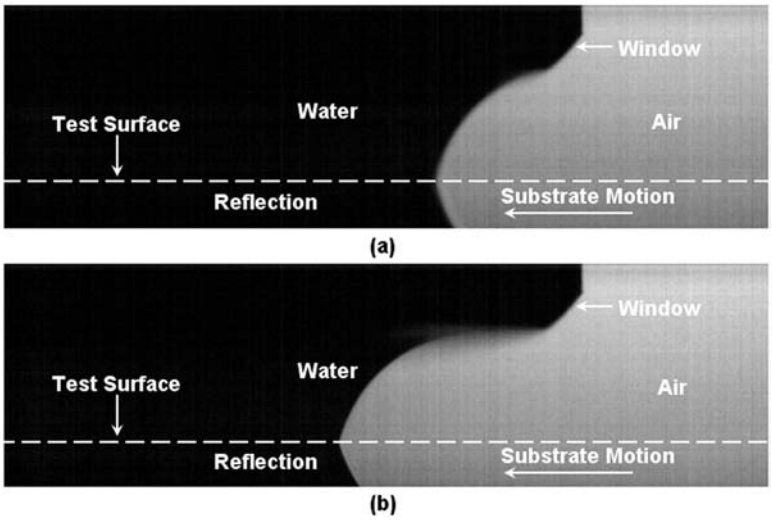

Figure 2.21: Sequential images of surface TOK TARF7047 with a velocity of 0.5 m/s. The fluid advances, leading to erroneous dynamic contact angle measurement.

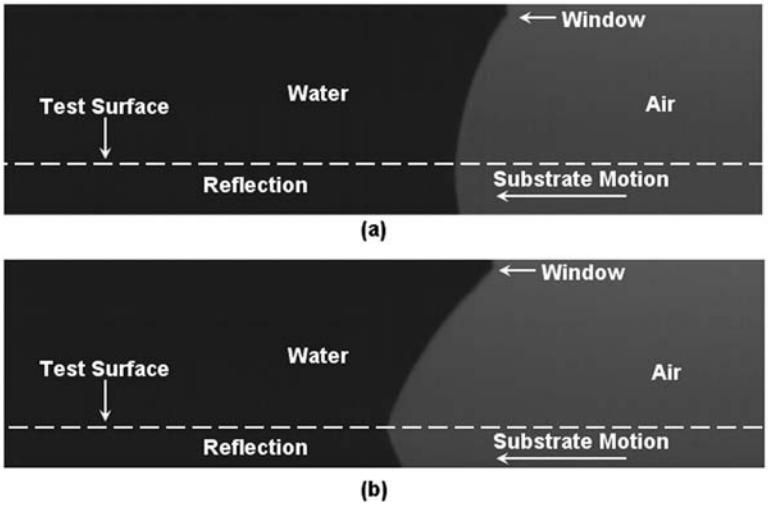

Figure 2.22: Images of surface Sumitomo PAR817 with a velocity of 0.01 m/s. (a) and (b) are different locations on the surface exhibiting distinct dynamic contact angles.

Chapter 3

Air Entrainment at the Contact Line

One of the challenges of immersion lithography is the possibility of having air bubbles within the immersion fluid. The curved gas/liquid interfaces that are associated with air bubbles will reflect and refract the incident light, distorting image patterns and decreasing yield. It is therefore critical that conditions which lead to the entrainment of air bubbles be avoided. There are three primary mechanisms that may result in the introduction of air bubbles in the immersion fluid at the contact line: (1) it is possible that the velocity of the contact line relative to the wafer may be sufficient so that a dynamic contact angle of 180° is achieved, (2) air may be trapped as the contact line advances over topographical features on the wafer, and (3) droplets of residual liquid that have been deposited on the wafer during previous scans may reencounter the meniscus and this collision may entrain air bubbles.

Air entrainment due to flow over topography and droplet-meniscus impact may become a problem for immersion lithography. These phenomena have been examined using both experimental visualization and CFD modeling.

3.1 Flow over Topography

The flow of the meniscus over microscale wafer topography may result in air entrainment through a fundamentally different mechanism than would be predicted by Voinov's equation and at a much lower velocity. This entrainment mechanism is shown in Fig. 3.1. The contact line may become attached to an edge of a sharp feature, effectively forcing the contact angle

towards 180° as the liquid above the attached contact line continues to be pushed forward by the bulk of the flow. The flow may pass over the feature before the meniscus reaches the bottom, leaving an unfilled region in the channel. The filling behavior is dominated by the contact angle; small differences in static contact angle can result in very different behavior. For example, CFD simulations performed by Wei [2004] predict that a 1000-nm wide feature that is 500 nm deep will be completely filled if the static contact angle is 60°, but will entrain air if the static contact angle is 75°.

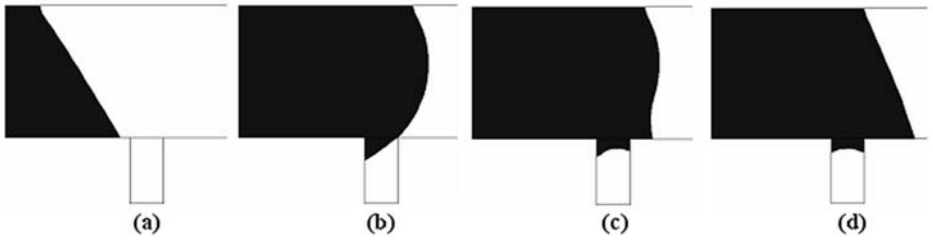

Figure 3.1: Progression of flow at a velocity of 1 m/s over a straight side-wall feature that is 250 nm-wide and 500 nm-deep, illustrating the mechanism by which air may be entrained: (a) flow on the hydrophilic surface approaches the feature, (b) during fill, the apparent contact angle is hydrophobic, (c) bulk of flow reaches opposite edge of feature causing the meniscus to rupture, and therefore (d) a pocket of air is entrained in the feature. [Wei, 2004]

3.1.1 Experimental Setup

To study the flow over topography in conditions that are relevant to immersion lithography, a fluid dispense and recover system (sometimes referred to as a "shower head") has been constructed. A side-view schematic of the system is shown in Fig. 3.2 and a bottom-view is shown in Fig. 3.3. This system allows experiments to be conducted in which a moving wafer mounted on a motorized stage assembly is dragged under a stationary meniscus at velocities up to 1 m/s. The fluid dispense and recover system provides a continuous flow of liquid through the lens-wafer gap even in the absence of wafer motion.

Fluid can be dispensed at flow rates up to 500 ml/min either through the injection

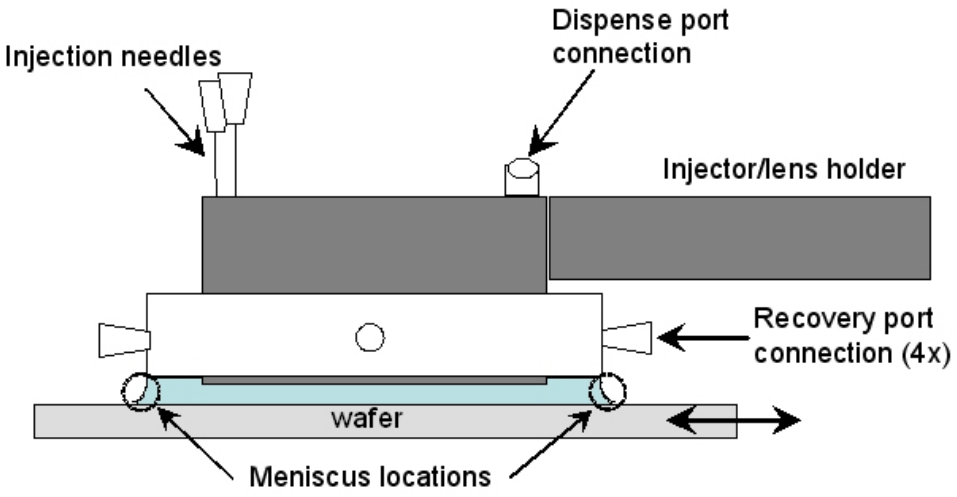

Figure 3.2: Side-view schematic of simultaneous fluid dispense and recover system.

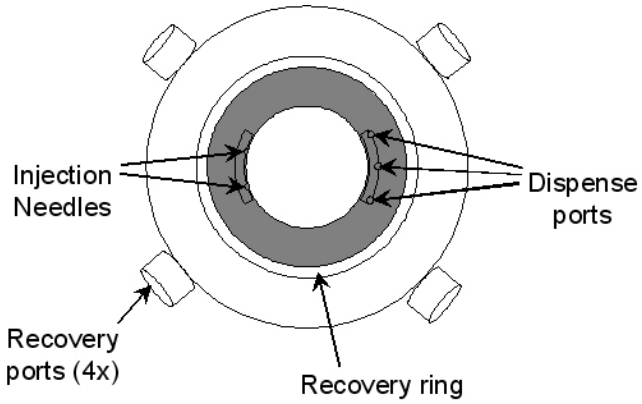

Figure 3.3: Bottom-view schematic of simultaneous fluid dispense and recover system.

needles, through three dispense ports, or both. A fluid recovery ring surrounds the lens region and has four connections leading to a recover line. A vacuum of up to 30 in. Hg can be applied to the recover lines. A close-up of the fluid management shower head can be seen in Fig. 3.4. The dispense and recover assembly is positioned over a moving substrate. The CMOS high-speed camera is mounted below the assembly and the meniscus is viewed through the glass substrate, as shown in Fig. 3.5. The system is activated by a peristaltic pump and a vacuum pump in a continuous, closed-loop manner.

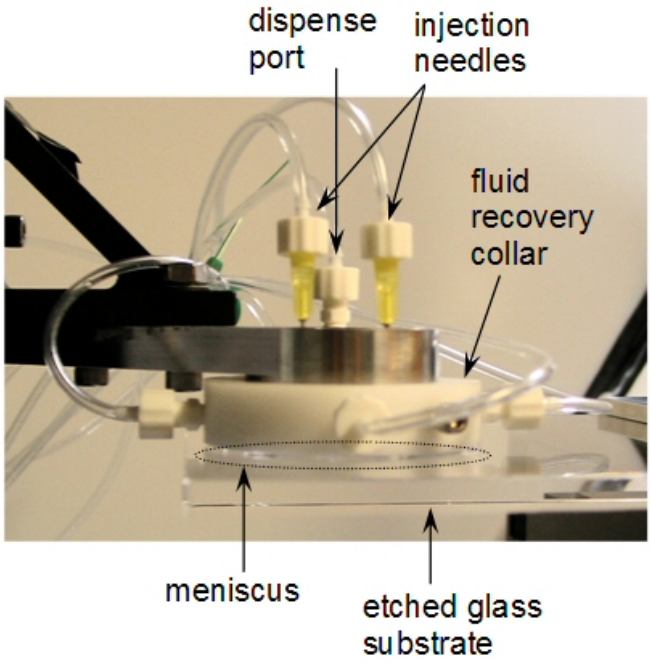

Figure 3.4: Close-up photo of fluid dispense and recover system.

3.1.2 Results

Figure 3.6 illustrates an image taken after bubbles have been injected into the fluid. Notice even very small bubbles (down to the smallest bubbles that were present, 7.3 μm in Fig. 3.6) are clearly visible. The same imaging system was previously shown to be capable of detecting bubbles down to 1 μm, verifying the ability of the imaging system to detect air entrainment at the micron scale [Switkes et al., 2004].

A number of line-space patterns were etched in a quartz substrate as seen in Fig. 3.7. The depth of all grooves was 0.5 μm whereas the width varied from 1.0 μm to 2.0 μm and the pitch varied from 0.6 μm to 10 μm. The array of patterns is listed in Table 3.1. In terms of the potential for air entrainment, the worst-case pattern on the substrate was the 1.0 μm wide, 0.5 μm deep lines with a 1.0 μm spacing. Figure 3.8 shows images of a 600-μm square segment of this pattern just before and immediately after the substrate was pulled under the water meniscus with a velocity of 1.0 m/s. Notice that in the figure on the right there is no

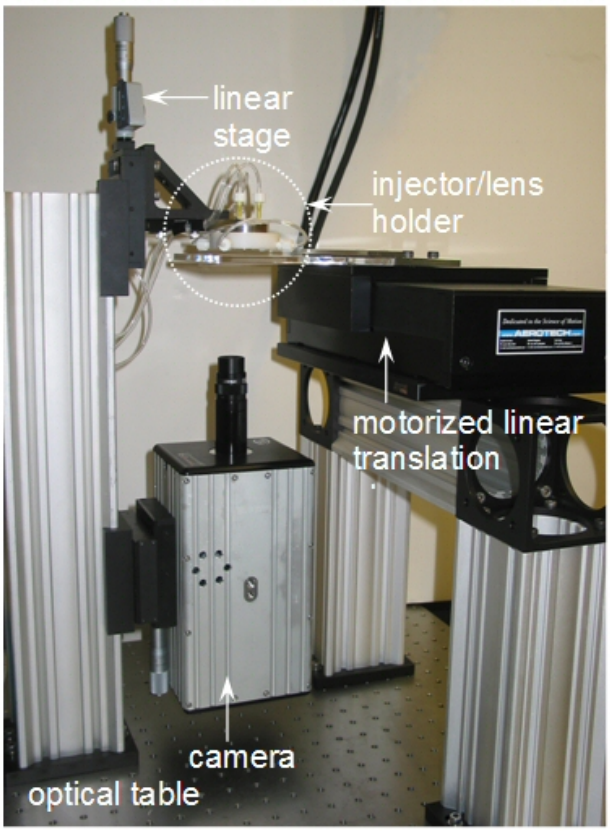

Figure 3.5: Photo of fluid dispense and recover system with camera and motorized linear stage.

evidence of any air entrainment.

3.1.3 Comparison with CFD

The progression of a flow over sharp-edged, vertical-sidewall features with 0.5 μm depth was investigated using CFD modeling via the technique described by Wei et al. [2004]. Fig. 3.9 illustrates a map of the results presented in the parameter space of feature width and contact angle. The regions in which the feature is completely filled and clearly entrains air are both indicated; note that hydrophobic and deep features tend to entrain air. Also shown are the conditions associated with the various patterns on the test wafer. Note that no air entrainment is predicted by the CFD model for any of the patterns on the test substrate,

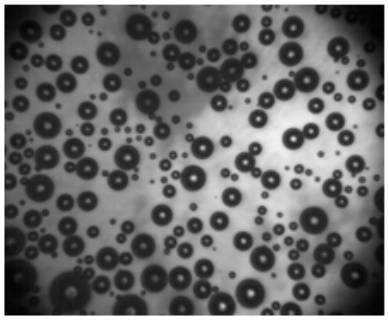

Figure 3.6: Image of water in which air bubbles have been injected, verifying the ability of the imaging system to detect micron-scale air entrainment.

Table 3.1: Etched quartz test mask with various line-space topography patterns.

	A	B	C	D	E	F	G	H
Line Width (μm)	0.6	1.0	1.5	2.0	0.6	0.6	0.6	0.6
Space Width (μm)	0.6	1.0	1.5	2.0	1.0	2.0	5.0	10.0
Number of Lines	400	200	200	200	2000	200	200	200

which is consistent with the experimental observation.

3.2 Droplet-Meniscus Impact

Droplets on the surface may lead to air entrainment in the immersion fluid. This may occur when an adhered droplet from a previous scan reencounters the advancing meniscus during subsequent scans.

3.2.1 Experimental Setup

The initial droplet impact investigation was conducted with a shower head (fluid dispense and recovery lens holder) in order to more closely mimic immersion lithography fluid conditions. However, due to the dynamic nature of the flow in this active fluid management system it was difficult to capture the effect of an individual droplet impact. As a result, a secondary setup was constructed that did not include an active fluid dispense system. Rather, a volume of

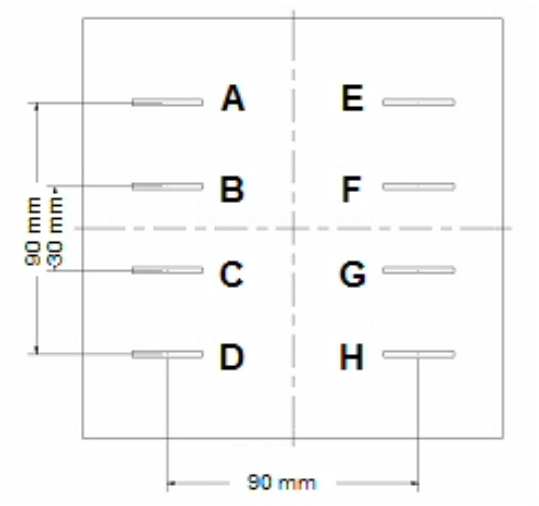

Figure 3.7: Etched quartz test mask with various line-space topography patterns.

liquid was contained between a test surface and a window. The camera was mounted above the substrate, looking down through the test surface onto a meniscus that was much more stationary and easier to visualize. An experimental investigation of the impact of droplets encountering the meniscus was conducted using this test facility, which is illustrated in Fig. 3.10.

In order to investigate air entrainment due to droplet impact on a μm-scale, the high-speed camera was used with a 20X microscope objective and small droplets were condensed onto the test surface. This was accomplished by cooling (using ice) the non-test side of the substrate while an ultrasonic humidifier provided a humid environment in the vicinity of the test surface. Condensate formed on the test surface, and the images of droplets impacting the meniscus were acquired as the substrate was subsequently advanced into the stationary meniscus. These data images were then examined for evidence of air entrainment. Rain-X-treated glass was selected as a worst case for possible bubble entrainment; it has been shown by CFD simulations of a droplet/meniscus impact that an impact of a droplet adhered to a hydrophobic surface is more likely to lead to air entrainment than a droplet on a

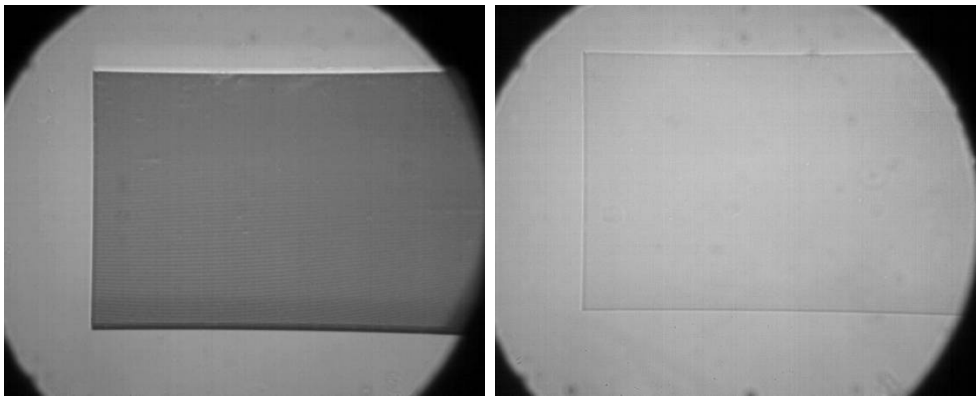

Figure 3.8: A 600-μm square image of the worst-case pattern on the etched quartz substrate, which consists of 1.0 μm wide lines with depth 0.5 μm on a 1.0 μm pitch just before (left) and after (right) the substrate was moved under the meniscus. Note that in the image on the right, the lines are immersed in water and there is no evidence of any air entrainment.

hydrophilic one. The test was conducted at a velocity of 1 m/s which is near the maximum velocity expected during immersion lithography; again, the high value of velocity was selected because the CFD simulations indicated that higher velocities increase the possibility of air entrainment.

Further investigation was conducted in which droplets of various sizes were deposited on Rain-X-treated glass and quartz surfaces using a syringe and injection needle. The surfaces were then advanced into the meniscus at velocities ranging from 0.01 to 1.0 m/s and high-speed video was taken at 628 Hz. There is a tradeoff between high magnification and the ability to keep the meniscus in the field of view as the substrate advances. For this reason, these experiments were conducted using a 5X microscope objective with the high speed camera to allow for a greater field of view. The 5X objective field of view is approximately 7.5×6.2 mm as compared to the 1.7×1.4 mm field of view with the 20X microscope objective.

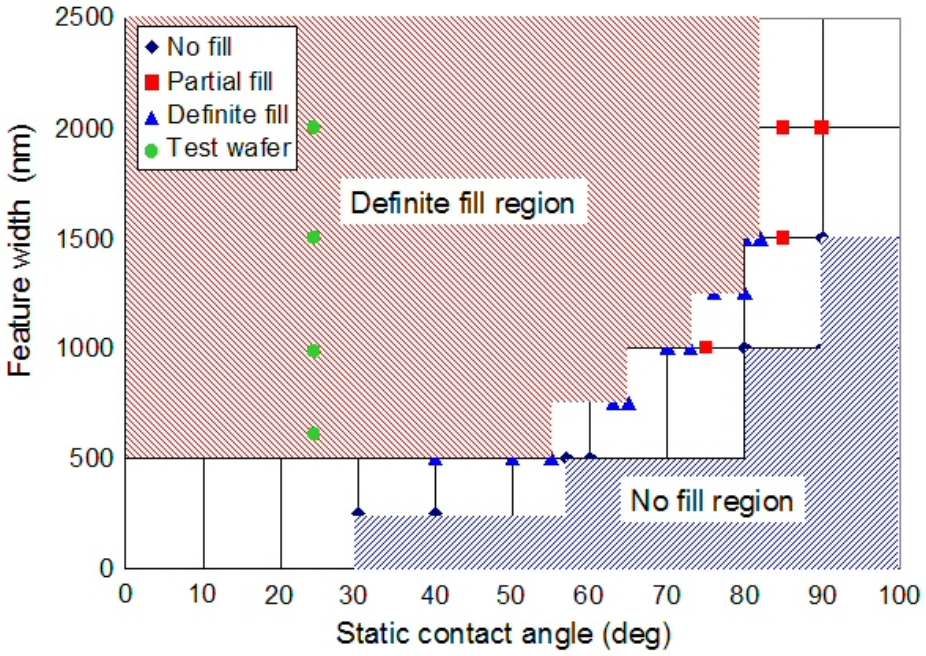

Figure 3.9: CFD results showing the regions in which air is entrained (the no-fill region) and in which the features fill (definite fill region) for 0.5 μm deep features in the parameter space of feature width and static contact angle. [Wei, 2004]

3.2.2 Results and Discussion

Images of the Rain-X-treated glass surface taken with the 20X objective are shown in Fig. 3.11. The condensate droplets range in size from 4-30 μm. The substrate was advanced into the meniscus at 1 m/s; no air entrainment was observed at this high magnification. However, three-dimensional CFD simulations of a meniscus advancing at a velocity of 1 m/s toward a stationary 50-μm droplet on a hydrophobic surface ($\theta_s = 120°$) led to air entrainment. Experiments on this scale did not show evidence of air entrainment; however, it may be that the optical system is unable to detect entrained air, as entrained bubbles are typically approximately 1/20th the size of their originating droplet. Therefore, micron and sub-micron scale bubbles would result; bubbles of this size are not detectable with the current optical setup. According to the bubble dissolution study presented by Shedd [2005], the expected bubble lifetime of 1-μm bubbles is less than 1 ms. In addition, the contact

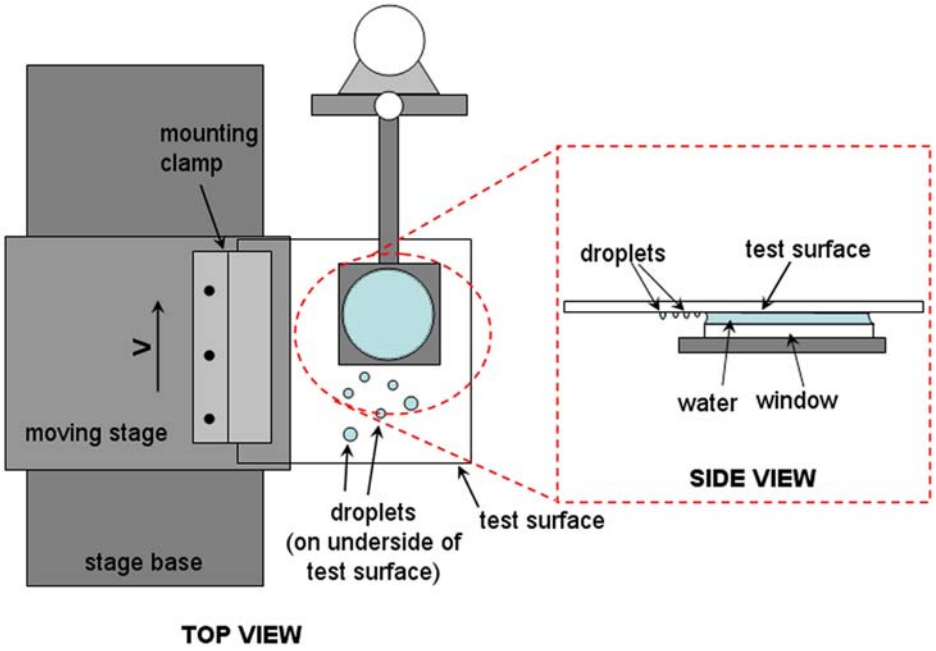

Figure 3.10: Top and side views of the experimental setup for droplet-meniscus impact experiments.

angle in the simulation exceeds that of the test surface, leading to an increased likelihood of air entrainment in the simulation than in the experiment. It is possible that air entrainment occurred but was not detected because the bubbles were too small.

On the Rain-X-treated surface, a set of data was taken with a 5X microscope objective and droplets that were deposited on the surface with a syringe. Test data was taken at 0.01 m/s velocity intervals from 0.01 to 0.1 m/s and at 0.1 m/s intervals up to a maximum velocity of 0.5 m/s. Data was unattainable at velocities in excess of 0.5 m/s as bulk fluid loss occurred. This meniscus overflow behavior is discussed further in Chapter 4. Air was entrained at the droplet-meniscus interface at all observed velocities. A series of data images showing entrained air bubbles are shown in Fig. 3.12. Droplets ranging in size from 260-3150 μm resulted in entrained bubbles ranging in size from 12-120 μm. No clear correlation between droplet size and bubble size was discernable.

A similar experiment was conducted on the quartz surface, using a 5X microscope ob-

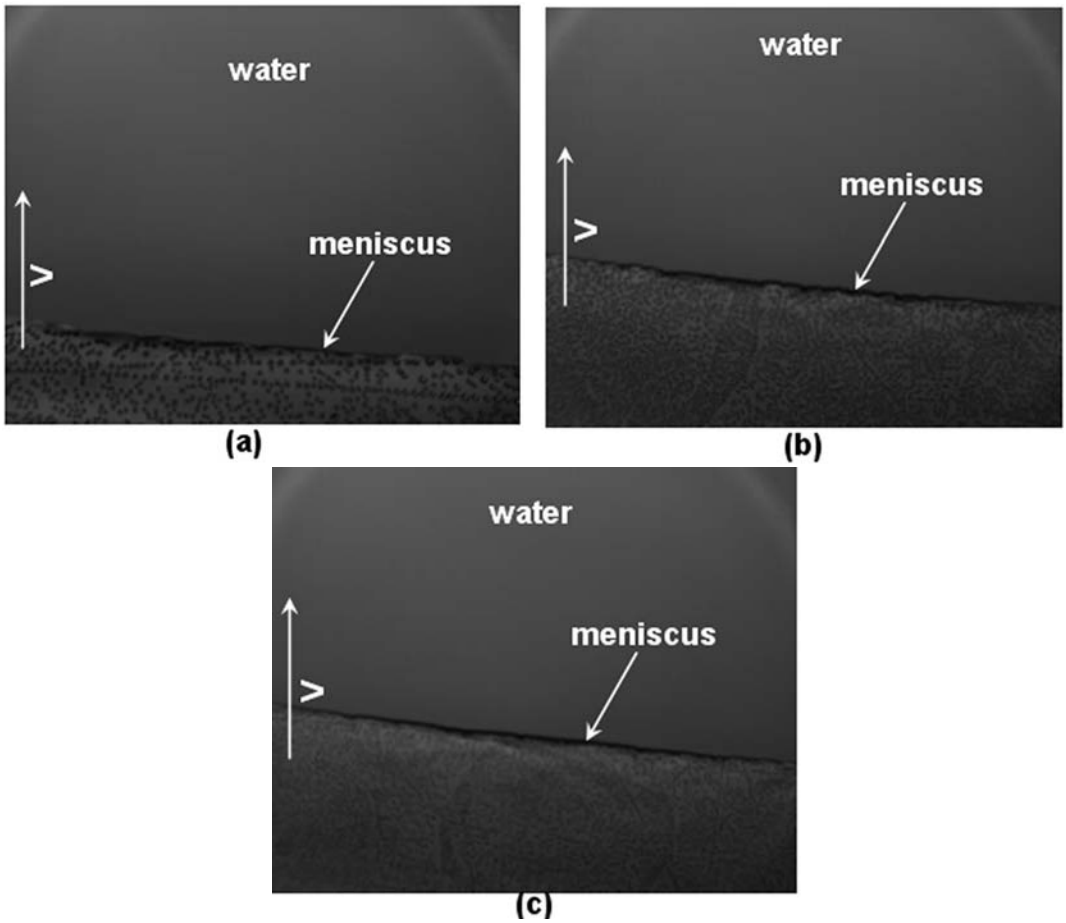

Figure 3.11: Droplets (4-30 μm) advancing into the meniscus at 1 m/s. Image (b) was taken 11 ms after image (a), and image (c) was taken 9.5 ms later.

jective and depositing droplets on the test surface with a syringe. Test data were taken at substrate velocities of 0.1 m/s intervals from 0.1 to 1.0 m/s. Air was not entrained at velocities below 0.8 m/s. Droplets ranging in size from 2400-5300 μm led to air entrainment at 0.8, 0.9, and 1.0 m/s. The largest droplet entrained a 225-μm bubble.

General Observations

For a given substrate velocity, drops of the same size do not consistently entrain bubbles at the meniscus interface. This could result from meniscus shape variability related to the memory of several droplets impacting the meniscus in succession and at random locations.

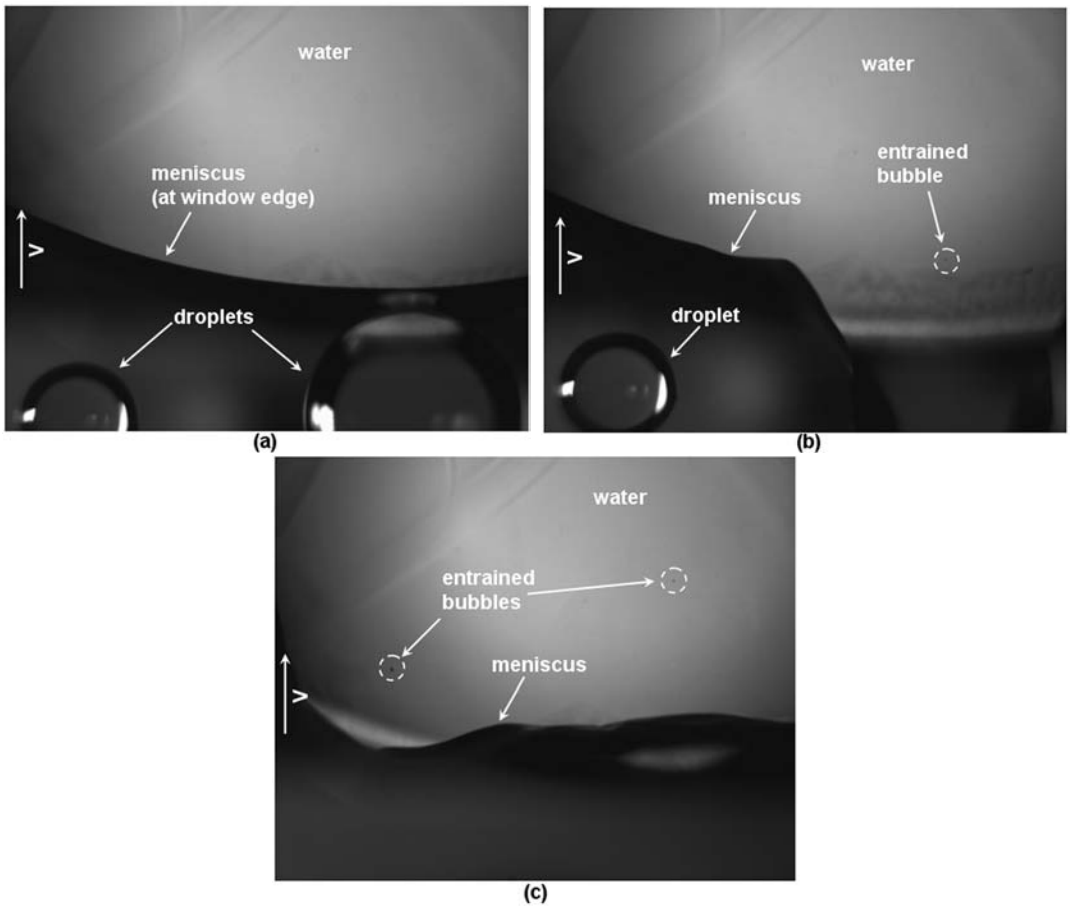

Figure 3.12: Data images taken as Rain-X treated glass is advanced into the meniscus at 0.2 m/s. Image (a) shows 2 droplets prior to meniscus impact. Images (b) and (c) show bubbles entrained by those droplets.

The meniscus shape is affected by the impacting droplets, causing meniscus motion and therefore changing the effective impact velocity that subsequent droplets experience. The impact angle of droplets may also be affected as the meniscus absorbs droplets and changes shape.

Care has been taken to distinguish between injected bubbles and air that is entrained due to droplet impact. Droplets that have been deposited on the test surface using a syringe and injection needle or a micropipette will often contain small bubbles. These will tend to be larger than entrained bubbles and will not originate from the droplet-meniscus boundary.

It should also be noted that occasionally entrained bubbles tend to stick to the substrate surface; air bubbles on the surface represent an especially important case for immersion lithography as they will be in the focal plane of the optical system during the scan.

In general, more bubbles are entrained at higher velocities. For a given droplet-meniscus impact, several bubbles may be entrained at higher velocity, where a single bubble is often entrained at lower velocity. Larger droplets appear to be more likely than smaller droplets to entrain air when impacting the meniscus.

Chapter 4

Receding Meniscus Behavior

It has been shown that droplet deposition on the surface may lead to air entrainment in the immersion fluid. This may occur when an adhered droplet from a previous scan re-encounters the advancing meniscus during subsequent scans. Any type of residual fluid left on the wafer is also of concern because it may evaporate, leading to the deposition of contaminants onto the surface. Surface contamination may lead to wafer defects, decreasing process yield. A schematic of a fluid management system illustrating the receding water/air meniscus explored in this chapter is shown in Fig. 4.1.

Three possible meniscus failure behaviors are observed as the wafer moves at constant velocity: meniscus overflow, thick film pulling, and thin film pulling; each of these mechanisms will result in the deposition of residual liquid onto the wafer surface. An experimental investigation characterizing these behaviors was conducted on quartz and Rain-X-treated glass substrates. These surfaces were selected because they have static contact angles of 44° and 100°, respectively, bracketing the wafer surface contact angles expected in immersion lithography. An engineering model of one of the failure mechanisms, referred to here as meniscus overflow, was developed. The engineering model is capable of predicting a critical velocity at which meniscus overflow occurs (i.e., the velocity at which there is a bulk loss of fluid from the lens-to-wafer gap). The critical velocity predicted by the model was compared with experimental observations.

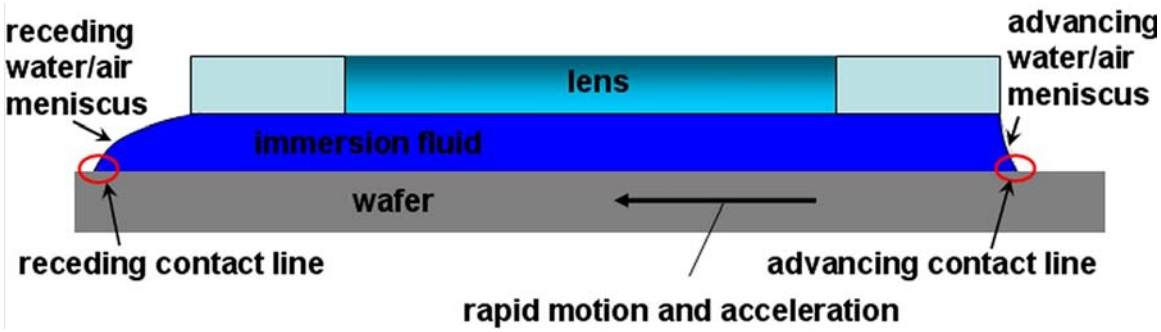

Figure 4.1: Side-view schematic of a fluid management system and associated menisci.

4.1 Engineering Model for Meniscus Overflow

Meniscus overflow occurs when the liquid in the lens-wafer gap does not remain adhered to the lens but rather tends to be pulled out of the gap by the wafer motion. The approximate pressure distribution within the meniscus is shown in Fig. 4.2. Note that the pressure tends to rise in the direction of the wafer velocity. This requires a sub-ambient pressure on the right-hand side of the bead and a pressure above ambient on the left-hand side of the bead. The difference in pressure between the fluid and ambient on either side must be sustained by the surface tension. This is reflected by changes in meniscus radius of curvature with changes in velocity.

The Couette velocity profile due to wafer motion requires that there be a net fluid flow from right to left. The pressure gradient generated by this flow forces an equal flow from left to right under the lens. An interface instability leading to meniscus overflow occurs when the front and receding interfaces cannot achieve sufficiently small curvature to sustain the viscous pressure rise. The critical velocity occurs when pressure jumps at the rear and advancing menisci are balanced by the viscous pressure rise. At steady-state, this can be expressed as

$$\frac{\gamma}{r_r} + \frac{\gamma}{r_a} = K_v \frac{\mu D V_w}{h^2} \tag{4.1}$$

where γ is the fluid surface tension, r_r is the radius of curvature of the meniscus at the

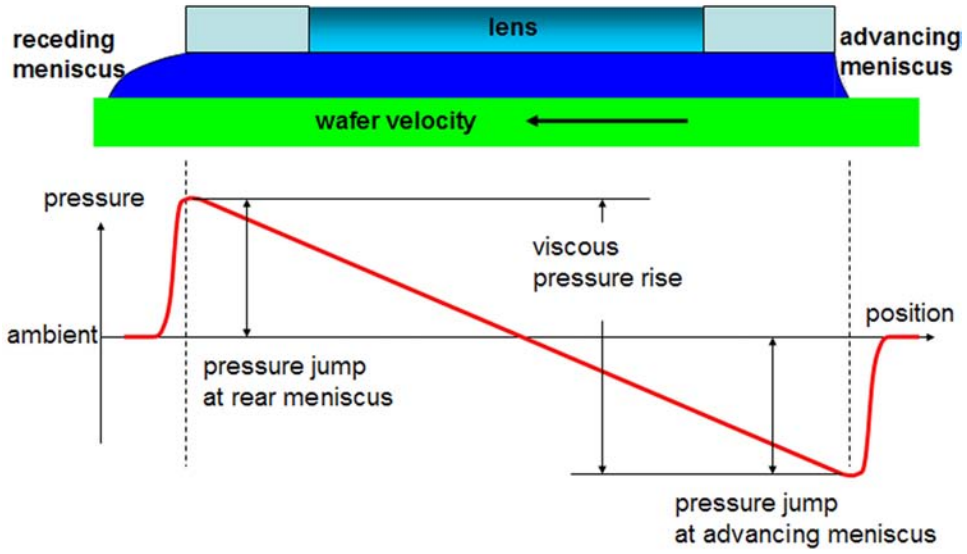

Figure 4.2: Side-view schematic of a fluid management system and associated pressures.

receding end, r_a is the radius of curvature of the meniscus at the advancing end, h is the gap height, μ is the viscosity of the fluid, D is the diameter of the lens, and V_w is the wafer velocity. The parameter K_v, the viscous pressure drop factor, is a dimensionless constant that depends on the configuration of the flow passage. It was approximated for the three-dimensional, circular gap using CFD simulations as described in the subsequent section. Equation (4.1) is valid only for steady-state wafer motion and there may be a significant additional pressure rise related to acceleration or deceleration effects.

4.1.1 Steady Viscous Pressure Rise Model

Fully-developed flow through an infinitely-wide gap with length L in which one surface is moving with velocity V_w is characterized by:

$$\frac{Q}{w} = \frac{V_w h}{2} - \frac{\Delta P h^3}{12 \mu L} \tag{4.2}$$

where Q/w is the flow rate per unit width of gap and ΔP is the pressure drop across the gap. In the absence of any flow, Eq. (4.2) simplifies to:

$$\Delta P = \frac{6L\mu V_w}{h^2} \tag{4.3}$$

Equation 4.3 indicates that a pressure rise is induced across the length of the gap. This pressure rise is proportional to the product of the gap length, plate velocity, and the fluid viscosity and inversely proportional to the gap height squared. In the simple case of an infinitely wide, two-dimensional gap, the constant of proportionality is exactly 6.0. However, for the more complex situation associated with flow driven laterally across a circular lens-wafer gap, as shown in Fig. 4.3, the constant of proportionality must be determined through CFD simulations.

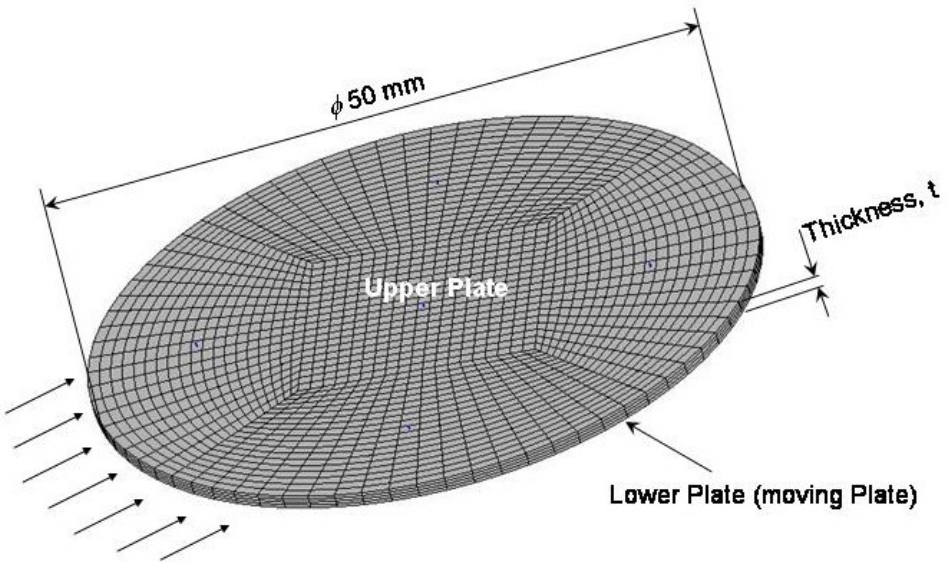

Figure 4.3: Circular lens-wafer gap in which the lower plate is moving.

Figure 4.4 illustrates the pressure contours in the circular fluid region predicted by a simulation in which the gap was 1.0 mm and the lower plate velocity was 1 m/s. Note that

the largest pressure rise occurs across the diameter of the lens and is nominally 250 Pa; this pressure difference will drive the meniscus overflow behavior.

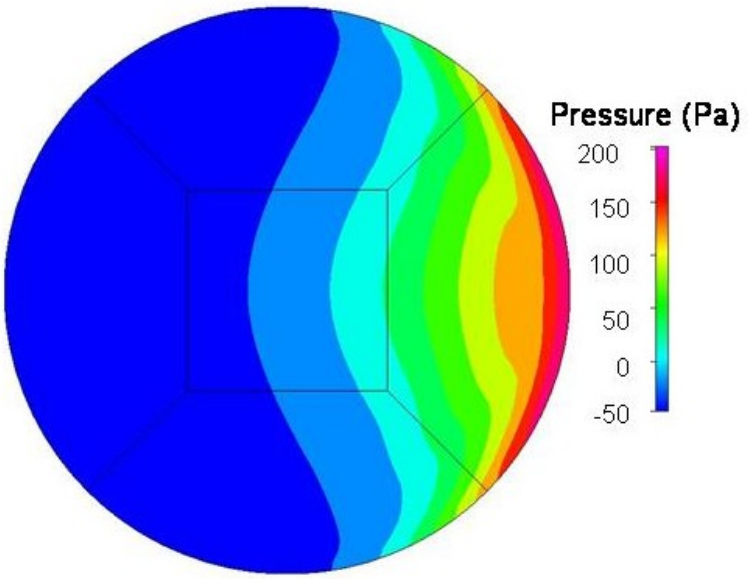

Figure 4.4: Pressure distribution within a 1 mm gap with a 1 m/s plate velocity.

Figure 4.5 illustrates the maximum pressure elevation as a function of the plate velocity for several gap height values. Note that the pressure rise is nominally linear with plate velocity but is a much stronger function of gap height, as indicated by Eq. (4.3).

The viscous pressure drop factor K_v is defined based on the scaling identified earlier:

$$K_v = \frac{h^2 \Delta P}{D \mu V_w} \tag{4.4}$$

Figure 4.6 illustrates the viscous pressure drop factor associated with the simulation results presented in Fig. 4.5 and indicates that $K_v = 4.75$ adequately represents the steady-state pressure rise for the conditions associated with immersion lithography.

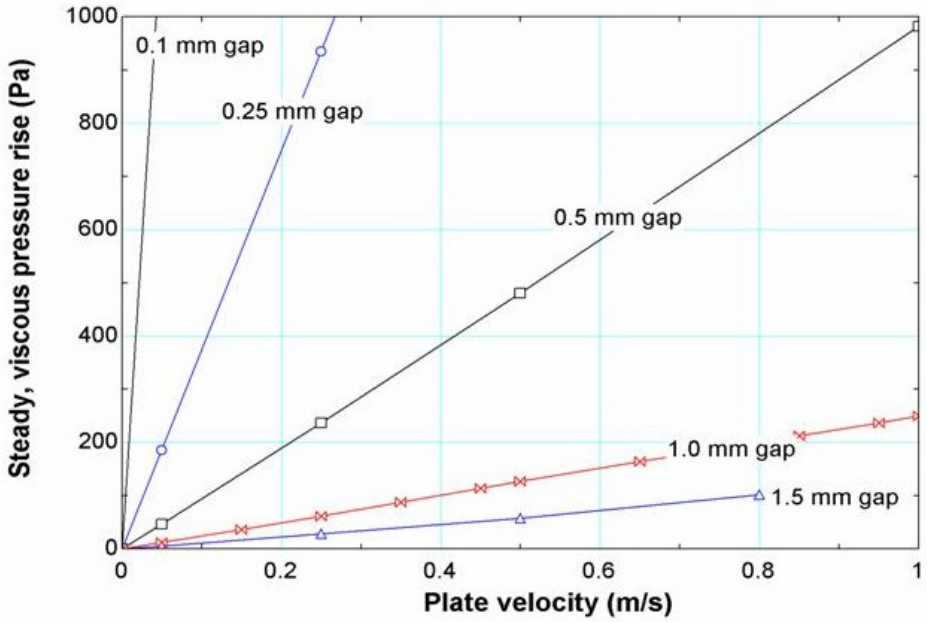

Figure 4.5: Maximum pressure elevation across a circular gap as a function of the plate velocity and for various values of the gap height.

4.1.2 Meniscus Shape Model

At velocities below the critical velocity, the receding meniscus adjusts via changes in radius of curvature to accommodate viscous pressure rise. This condition is preferred as it does not lead to loss of fluid from the lens-to-wafer gap or fluid deposition on the wafer surface. As the velocity increases and approaches the critical velocity, the radius of curvature at the receding meniscus will sometimes tend to decrease by forming a bulge. This "foot" of liquid is sometimes observed extending stably past the lens. This phenomenon is illustrated in Fig. 4.7.

Meniscus overflow occurs when the fluid escapes from the fluid management system gap because the viscous pressure rise overwhelms the stabilizing surface tension force. This occurs when the geometric limitations on the radius of curvature prevent further increase in this force. The critical velocity is the velocity just below that at which this takes place.

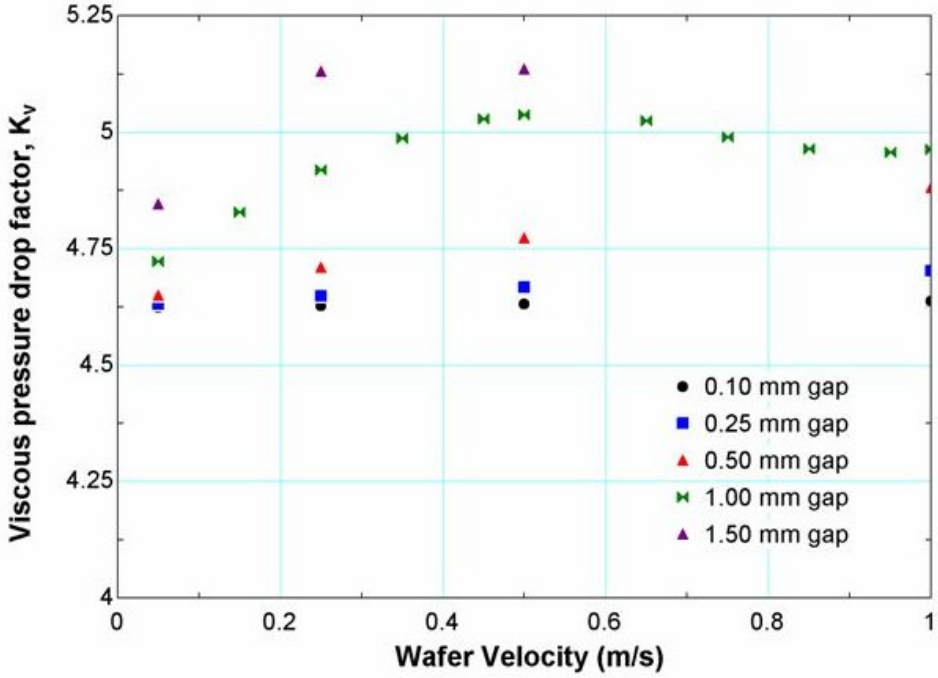

Figure 4.6: Viscous pressure drop factor associated with the CFD results.

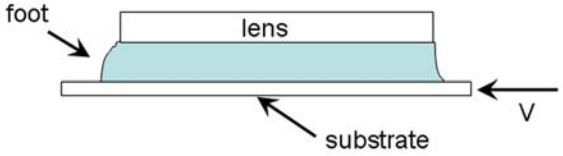

Figure 4.7: A schematic of "foot" behavior.

Figure 4.8 illustrates the progression of the interface shape as the velocity approaches critical velocity. Initially, at very low velocity, there is no pressure rise across the lens-to-wafer gap and therefore no countering surface tension force is required; the meniscus radius of curvature approaches infinity and the interface becomes a straight line between the pinning point at the edge of the fluid management surface and the wafer. The line satisfies the contact angle at the wafer, θ_r.

As the velocity increases, the meniscus is deformed so that there is a pressure jump across the meniscus, as shown in Fig. 4.2. The increased pressure jump results in a reduction in

the radius of curvature such that the interface is convex as seen by the fluid. The result is a gradual bowing out of the meniscus, as shown in Fig. 4.8.

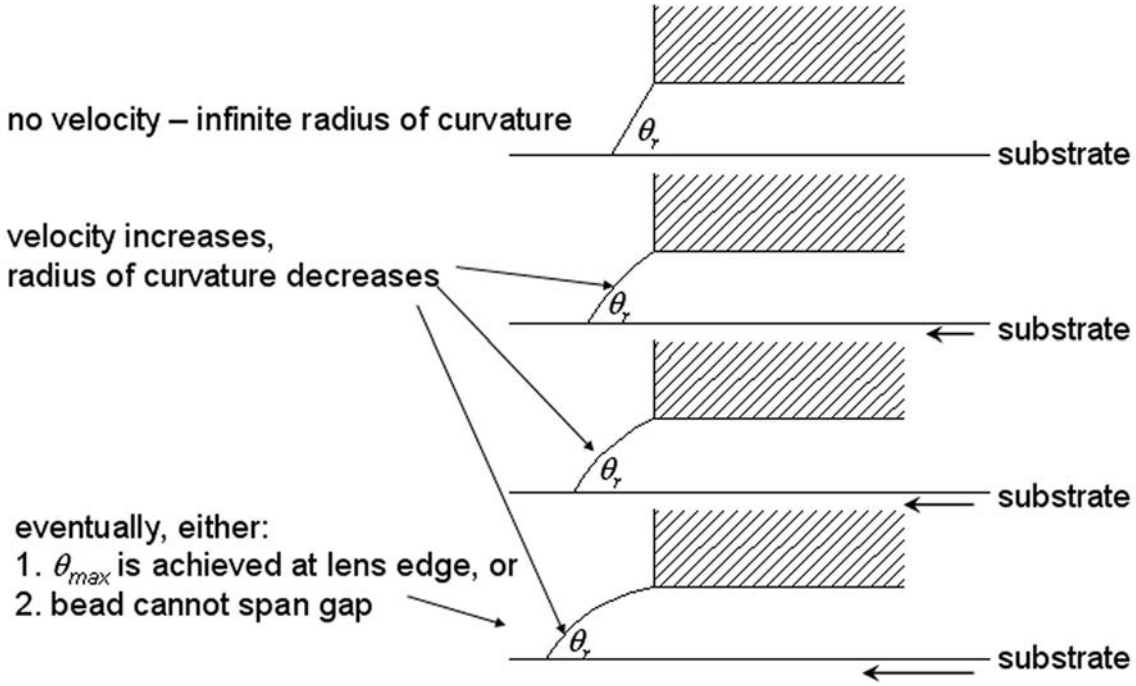

Figure 4.8: Receding interface adjusting to an increasing pressure within the fluid due to the wafer velocity.

Eventually, the pinned contact line may achieve the static, advancing contact angle with respect to the material at the side of the fluid management system and begin to climb up the side, immediately resulting in an increase in the radius of curvature and therefore meniscus overflow. The maximum ratio of gap height to radius of curvature that can be achieved in this limit is:

$$\frac{h}{r} = \cos\left(\theta_{m,a} - \frac{\pi}{2}\right) - \sin\left(\frac{\pi}{2} - \theta_{w,r,d}\right) \tag{4.5}$$

where $\theta_{m,a}$ is the static advancing contact angle associated with the fluid management system surface and $\theta_{w,r,d}$ is the dynamic receding contact angle associated with the wafer.

Alternatively, the fluid meniscus is eventually unable to both retain is circular shape and

span the gap, in which case it is stretched; this also results in an increase in the radius of curvature and therefore meniscus overflow. The maximum ratio of gap height to radius of curvature that can be achieved in this limit is:

$$\frac{h}{r} = 1 - \sin\left(\frac{\pi}{2} - \theta_{w,r,d}\right) \tag{4.6}$$

In either case, meniscus overflow occurs as shown in Fig. 4.9 and the fluid is no longer retained in the gap but tends to move with the wafer. Large amounts of residual liquid are left on the wafer after a meniscus overflow event.

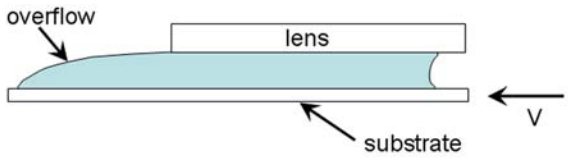

Figure 4.9: An illustration of meniscus overflow.

Equations (4.5) and (4.6) describe the surface tension force that can be achieved at the receding meniscus. The advancing meniscus also plays a role in meniscus overflow, as indicated by Eq. (4.1). Figure 4.10 illustrates how the shape of the advancing meniscus is affected by increasing velocity.

As the velocity increases, the advancing meniscus changes shape from linear (i.e., having an infinite radius of curvature) to convex, as viewed from the liquid. Eventually either the static receding contact angle is achieved at the lens surface or the interface cannot maintain a circular shape and span the gap. In the first limit, the ratio of the gap height to radius of curvature is given by:

$$\frac{h}{r} = \sin\left(\frac{\pi}{2} - \theta_{m,r}\right) + \sin\left(\frac{\pi}{2} - \theta_{w,a,d}\right) \tag{4.7}$$

where $\theta_{m,r}$ is the static receding contact angle associated with the fluid management system surface and $\theta_{w,a,d}$ is the dynamic advancing contact angle associated with the wafer. In the

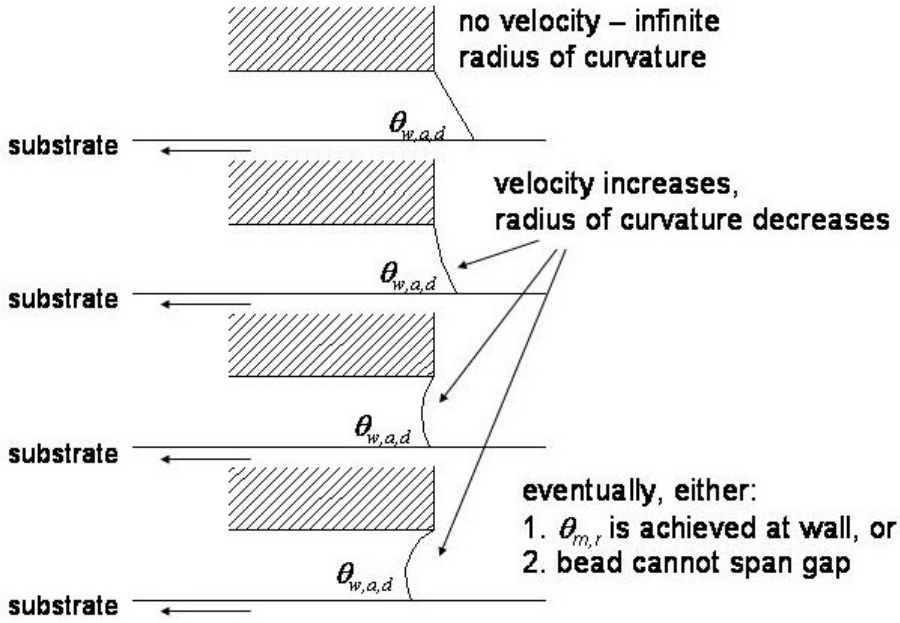

Figure 4.10: The advancing meniscus shape as velocity increases.

second limit, the ratio of the gap height to radius of curvature is given by:

$$\frac{h}{r} = 1 + \sin\left(\frac{\pi}{2} - \theta_{w,a,d}\right) \tag{4.8}$$

Equations (4.5) to (4.8) were derived based on geometry and fail to account for the effect of fluid pressure or flow on the interface shape. To verify that these equations adequately capture the surface tension force, CFD models were generated. Figure 4.11 illustrates the CFD model; a stationary wafer and fluid management system with a sharp edge were considered. The gap between these surfaces was initially filled with liquid and the pressure just inside the gap was gradually increased or decreased relative to ambient in order to simulate the receding or advancing meniscus, respectively.

The pressure elevation at which the meniscus becomes unstable and overflows is compared to the pressure jump predicted by the minimum of Eqs. (4.5) and (4.6). The pressure

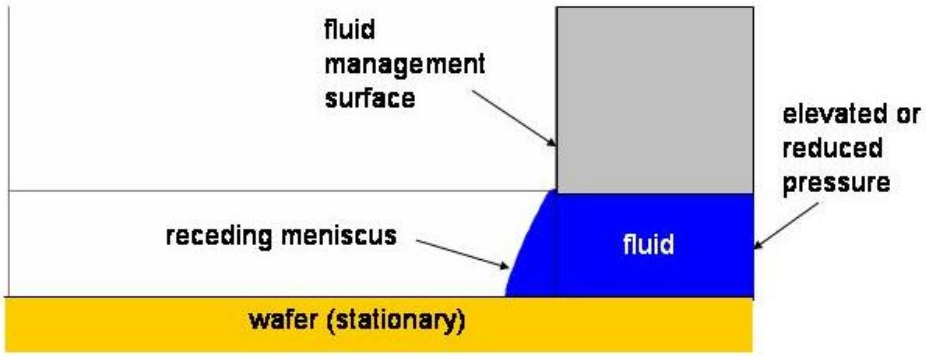

Figure 4.11: CFD model used to verify the pressure jump equations.

reduction at which the meniscus becomes unstable and is pulled into the gap is compared to the pressure jump predicted by the minimum of Eqs. (4.7) and (4.8). The CFD results and geometric model predictions are shown in Fig. 4.12 as a function of the contact angle (assumed to be the same for both the wafer and fluid management surface). Reasonable agreement is observed; the scatter in the CFD results is likely due to the qualitative nature of defining the onset of instability or inertial effects associated with accelerating the fluid.

4.1.3 Film Pulling Model

The dynamic contact angle that characterizes the intersection of the receding meniscus with the wafer is reduced as the wafer velocity increases. When the dynamic contact angle approaches zero, a very thin film of liquid will be "pulled" from the receding meniscus. This behavior is illustrated in Fig. 4.13, and is most easily observed on hydrophilic surfaces. This failure mechanism is not as extreme as meniscus overflow; however, undesirable droplets of liquid are deposited on the substrate surface.

Several researchers have presented correlations that describe the variation of the dynamic contact angle with velocity. Immersion lithography will be characterized by relatively large

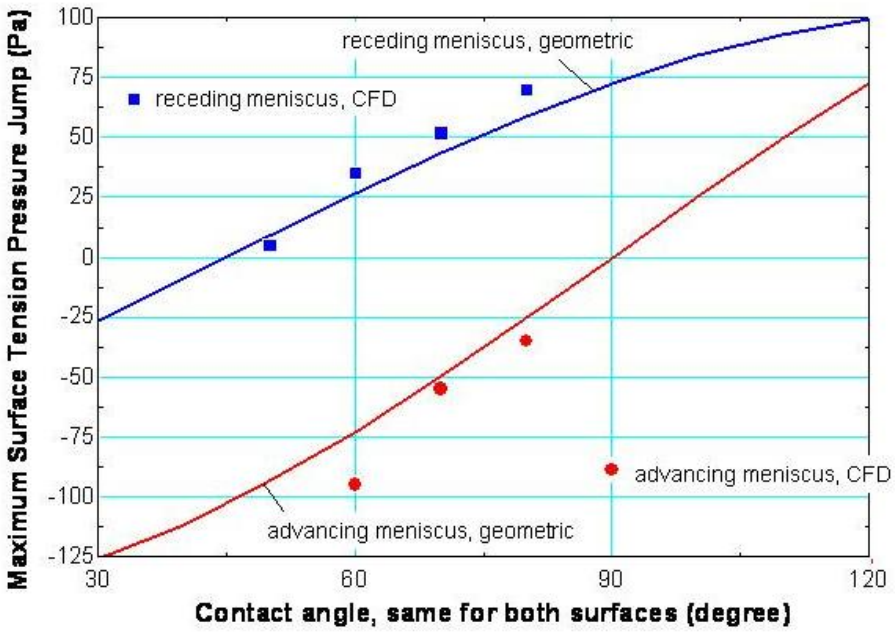

Figure 4.12: Pressure jump across meniscus at the onset of instability; as predicted by the geometric models and the CFD simulation.

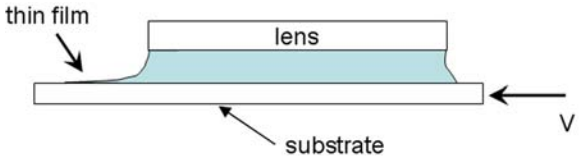

Figure 4.13: A schematic of thin film pulling behavior.

Reynolds numbers and large accelerations, and therefore most previous work in the area of film pulling for coating technologies is not directly applicable. However, correlations for the receding, dynamic contact angle under idealized and inertia-free conditions have been shown to be nominally accurate and therefore it is possible to approximately predict the onset of film-pulling using Voinov's equation [Petrov et al., 1992] by setting the dynamic contact angle to zero:

$$V_w = \frac{\gamma \theta_{s,r}^3}{9\mu \left[\ln \frac{h}{L_s} + C\right]} \tag{4.9}$$

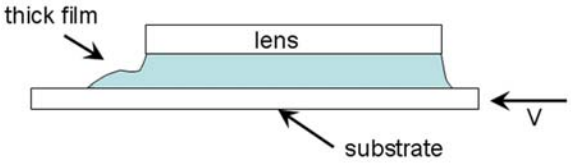

Figure 4.14: A schematic of thick film pulling behavior.

where $\theta_{s,r}$ is the static, receding contact angle.

Under some conditions it has been observed that a thick film is pulled from the receding meniscus, as illustrated in Fig. 4.14. The thickness of the film is much larger than the film pulled as the dynamic contact angle approaches zero. The cause of this failure is not well understood; however, the situation appears to exhibit hysteresis. It is likely that the local curvature of the meniscus provides the pressure gradient that is required to balance the Couette flow driven by the wafer motion.

4.1.4 Acceleration Pressure Elevation Model

A pressure elevation is generated across the length of the gap at the conclusion/initiation of each wafer oscillation that is related to the deceleration/acceleration of the immersion fluid. This pressure elevation can be comparable to the steady-state viscous pressure rise considered in Sec. 4.1.1. Figure 4.15 illustrates the anticipated wafer velocity as a function of time for one back-and-forth scanning operation. The wafer velocity is characterized by a steady-state scan velocity, u_{scan}, and scan time, t_{scan}, as well as an acceleration rate, a.

In order to consider the impact of the acceleration and oscillatory motion on the meniscus overflow behavior, a one-dimensional (1D), transient finite difference model has been developed that is capable of predicting the pressure gradient as a function of time. The model is fully implicit and solved via a single, sparse matrix decomposition operation.

The governing equation for this problem is the Navier-Stokes equation simplified by

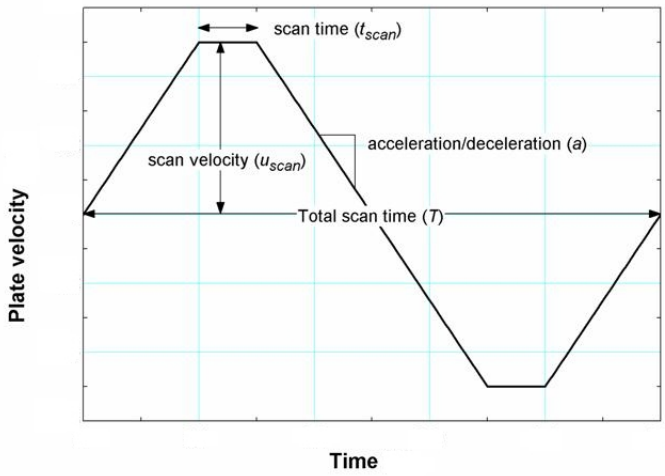

Figure 4.15: Wafer velocity as a function of time.

eliminating the negligible viscous terms and the inertia terms:

$$\rho\frac{\partial u}{\partial x} = -\frac{\partial p}{\partial x} + \mu\frac{\partial^2 u}{\partial y^2} \tag{4.10}$$

where ρ is the density of the immersion fluid, u is the x-directed velocity, x is the direction parallel to the surface of the wafer and y is perpendicular to the wafer. The boundary conditions used to solve this equation follow. The velocity at x=0 must be the wafer velocity, u_w, shown in Fig. 4.15.

$$u(y = 0, t) = u_w(t) \tag{4.11}$$

The velocity at the top of the gap is always zero:

$$u(y = h, t) = 0 \tag{4.12}$$

The fluid must undergo a cyclic steady-state; that is, the velocity distribution at the conclusion of any scan (at time t=T in Fig. 4.15) must be the same as the velocity distribution

at the initiation of the scan (at time t=0).

$$u(y, t = T) = u(y, t = 0) \tag{4.13}$$

Finally, the flow through the gap must be equal to the externally-forced flow rate. The externally-forced flow is zero in the case shown in Fig. 4.2; however, in general, the bulk flow rate through the gap may be finite, u_{flow}.

$$\frac{\int_0^h u(y,t)dy}{h} = u_{flow} \tag{4.14}$$

The solution is obtained over a grid that extends over space (from the wafer to the gap) and time (from t=0 to t=T), as shown in Fig. 4.16.

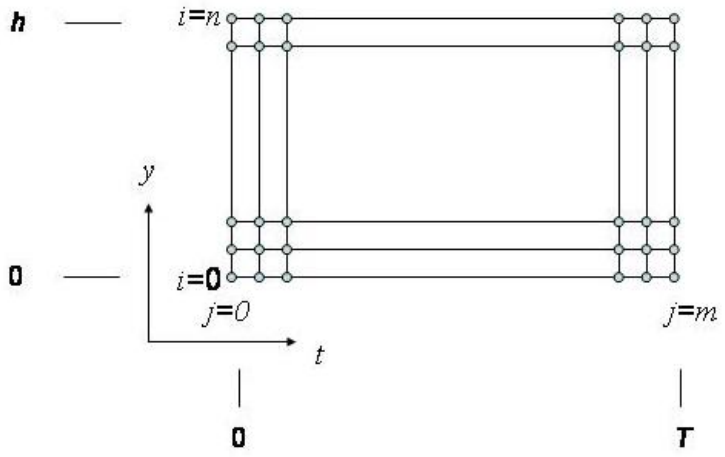

Figure 4.16: Numerical grid used to determine the velocity within the gap during the wafer oscillation.

The discretized form of the governing equation, using the grid illustrated in Fig. 4.16 is:

$$u_{i,j}\left[\frac{2\mu}{\Delta y^2}\right] + u_{i-1,j}\left[-\frac{\mu}{\Delta y^2}\right] + u_{i+1,j}\left[-\frac{\mu}{\Delta y^2}\right] + u_{i,j-1}\left[-\frac{\rho}{\Delta t}\right] + \left(\frac{\partial p}{\partial x}\right)_j = 0 \tag{4.15}$$

Equation (4.15) is written for nodes i=1..(n-1) and j=1..m where n and m are the number of spatial and temporal nodes, respectively. The boundary conditions are enforced at the remaining nodes. The moving plate velocity is enforced for nodes i=0 and j=0..m:

$$u_{i=0,j} = u_w(j\Delta t) \tag{4.16}$$

The stationary wafer is enforced for nodes i=n and j=0..m:

$$u_{i=n,j} = 0 \tag{4.17}$$

Cyclic steady state is enforced for nodes i=1..(n-1) and j=0:

$$u_{i,j=0} = u_{i,j=m} \tag{4.18}$$

and also for the pressure gradient:

$$\left(\frac{\partial p}{\partial x}\right)_0 = \left(\frac{\partial p}{\partial x}\right)_m \tag{4.19}$$

Finally, the forced fluid velocity is enforced according to:

$$\sum_{i=0}^{n} u_{i,j}\Delta y = hu_{flow} \text{for } j = 1..m \tag{4.20}$$

Equations (4.15) to (4.20) represent a system of $(n + 1) \times (m + 2)$ unknowns. The unknowns are the velocities at each node ($u_{i,j}$) and the pressure gradient at each time $\left(\frac{\partial p}{\partial x}\right)_j$. These linear equations are solved using a single, sparse matrix decomposition. Figure 4.17 shows the velocity as a function of position at various times for the wafer velocity variation shown in Fig. 4.15 and no forced flow ($u_{flow} = 0$).

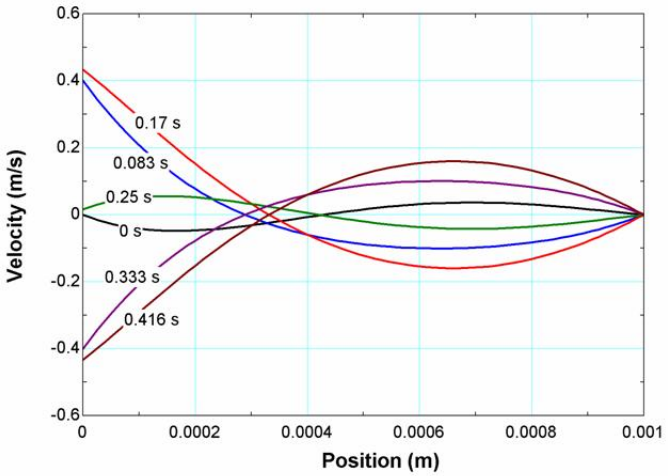

Figure 4.17: Velocity as a function of position at various times during a scan.

Note that there is a clear time lag at various locations related to the inertia of the fluid; the velocity at $y = 0.7$ mm is almost completely out-of-phase with the wafer velocity. Figure 4.18 illustrates the pressure gradient as a function of time associated with the velocity distribution shown in Fig. 4.17. Note that the pressure gradient eventually reaches the steady-state pressure gradient predicted by Eq. (4.3); however, the acceleration and deceleration results in spikes in the pressure gradient that exceed this steady-state pressure gradient. The excess pressure gradient, $\frac{\partial p}{\partial x}\Big)_{acc}$ in Fig. 4.18, is shown in Fig. 4.19 as a function of the acceleration for various gap heights assuming a scan velocity of 1.0 m/s and a scan time of 50 ms. Note that the effect of the increasing acceleration is to increase $\frac{\partial p}{\partial x}\Big)_{acc}$. Also, decreasing the gap height results in an increase in the acceleration-induced pressure gradient because the increased viscous force tends to more strongly link the fluid motion to the wafer motion.

In order to facilitate the integration of the finite-difference model with the engineering model, the acceleration-induced excess pressure gradient is non-dimensionalized (P_a) against the inertially-induced pressure gradient that would result from the entire fluid moving with

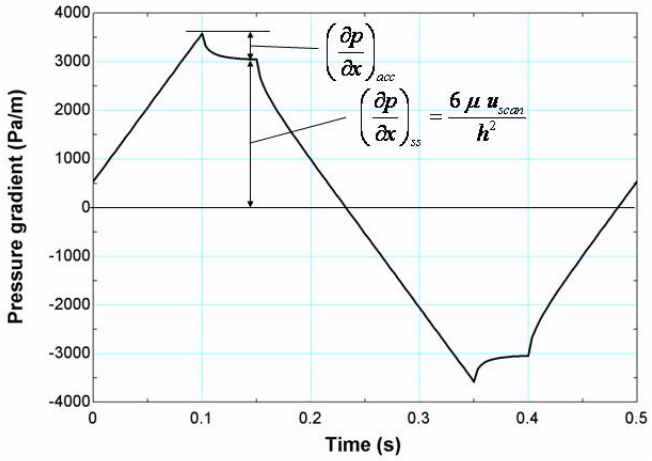

Figure 4.18: Pressure gradient as a function of time during a scan.

the wafer:

$$P_a = \frac{\left(\frac{\partial p}{\partial x}\right)_{acc}}{\rho a} \tag{4.21}$$

The gap height is non-dimensionalized (H) against the momentum penetration depth that associated with the acceleration process:

$$H = \frac{h}{\sqrt{\frac{\mu u_{scan}}{\rho a}}} \tag{4.22}$$

Figure 4.20 illustrates the nondimensional, acceleration-induced pressure gradient (P_a) as a function of the nondimensional gap height (H) for the conditions illustrated in Fig. 4.19. Note that these data collapse and indicate that the nondimensional pressure gradient can be expressed approximately as a function of nondimensional gap height. The curve fit to the data is:

$$P_a = exp(-\frac{H}{0.467936}) + \frac{0.142428}{H^{0.159588}} \tag{4.23}$$

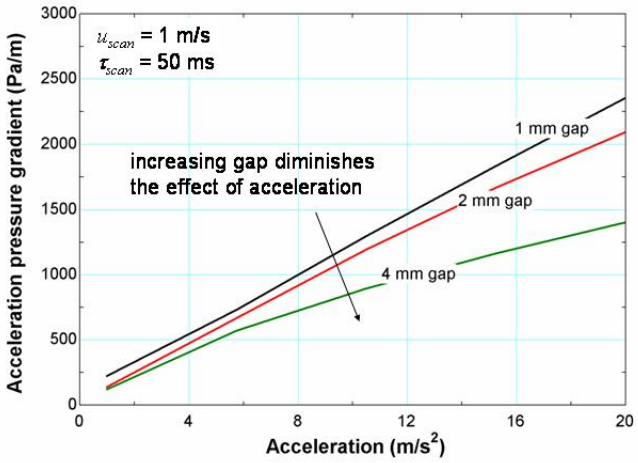

Figure 4.19: Acceleration induced, excess pressure gradient as a function of acceleration for various values of the gap height.

4.2 Experimental Setup

The initial experimental setup featured a fluid management system with an inboard dispense ring surrounded by an outer recovery ring, as seen in Fig. 4.21. This representative immersion lithography shower head system incorporated continuously circulating flow. If the flow rates on the left and right hand sides are assumed to be equal, then the flow rate driven pressure term that would be an additional term in Eq. (4.1) will be equal and opposite on the two sides of the lens; this term will therefore not contribute to the pressure rise between the right-hand and left-hand sides of the bead:

$$\Delta P_Q = \frac{12\mu Q L_1}{wh^3} \tag{4.24}$$

This is consistent with the experimental observation that the results were independent of circulating flow rate. For this reason, and to simplify the study of meniscus behavior, only the case without externally imposed flow is examined. This also eliminates any possible

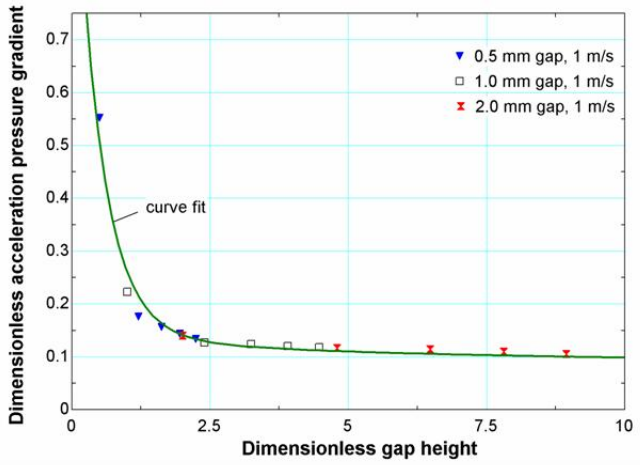

Figure 4.20: Acceleration induced, excess pressure gradient as a function of acceleration for various values of the gap height.

meniscus wobble, which had been observed with circulating flow and has unknown effects.

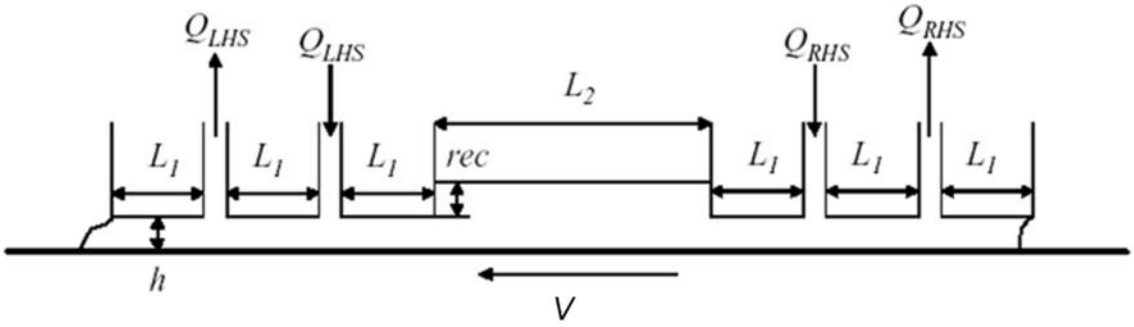

Figure 4.21: A schematic that represents the initial experimental test facility.

To study meniscus overflow and film pulling, and validate the engineering model, a system with a nominally static and stationary meniscus was constructed. The test facility illustrated in Fig. 4.22 consists of an adjustable gap between a test surface that is affixed to a motorized linear stage and a 2.0 in. circular quartz window that is mounted to a vertical stage positioned with a digital micrometer. For ease of fabrication, the facility was constructed such that the test surface is above the window, that is "upside-down" with respect to the previous

illustrations. A photograph of the test facility is shown in Fig. 4.23. At the gap heights and velocities investigated, changes in orientation with respect to gravity did not appear to modify observed meniscus behavior, which is consistent with the very small Bond number (Bo) characterizing the experiment.

$$Bo = \frac{g\rho h^2}{\gamma} \tag{4.25}$$

where g is gravity. The Bond number for a gap height of 1.0 mm is approximately 0.1.

Water was manually injected between the test surface and the quartz window prior to each data acquisition series using a syringe and injection needle. Meniscus behavior was observed for a range of gap heights and velocities by imaging the meniscus edge with a high-speed camera as the substrate was advanced into the fluid. Steady-state behavior, acceleration effects, and deceleration effects were recorded. The test surface and window were matched: when using a Rain-X-treated test surface, the window was also treated with Rain-X; likewise when using a quartz test surface, an untreated quartz window was used.

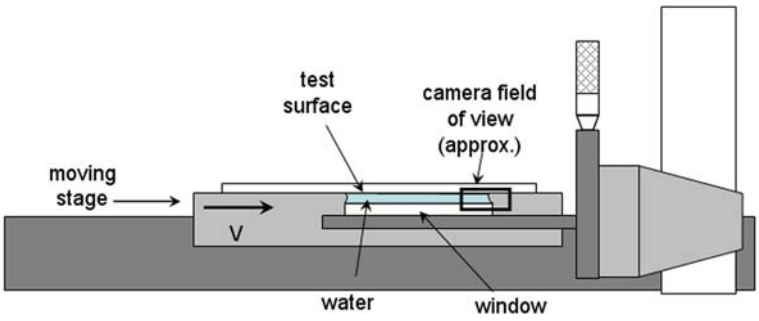

Figure 4.22: A schematic of the test facility for study of meniscus behavior.

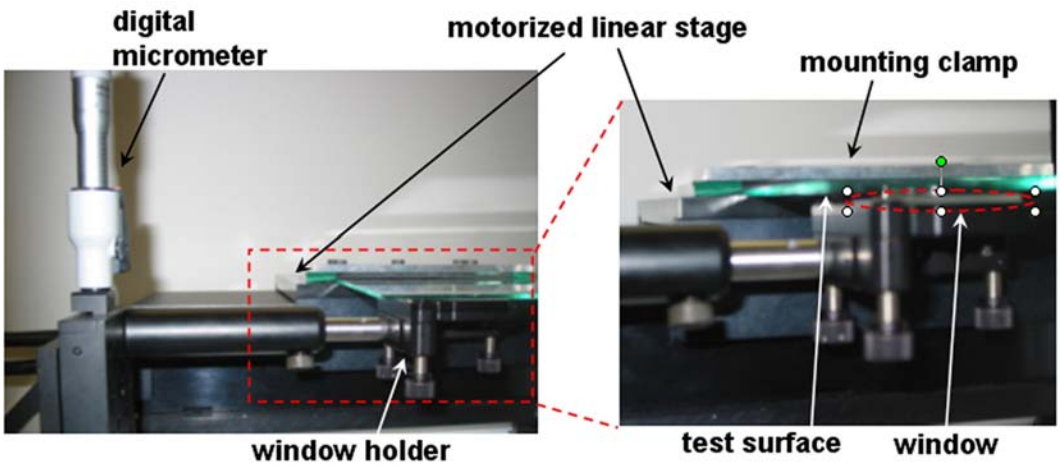

Figure 4.23: A photograph with close-up (right) of the test facility for study of meniscus behavior.

4.3 Results and Discussion

4.3.1 Rain-X-treated Glass Substrate

Data images were acquired by Rodríguez [2004] at various velocities and gap heights with a Rain-X-treated glass substrate. The substrate velocity was varied from 1-500 mm/s while the gap height ranged from 0.71 to 2.46 mm. Results depicting the qualitative behavior can be seen in Fig. 4.24. An image exemplifying the "no meniscus overflow" condition is shown in Fig. 4.25. The meniscus behavior transitions from no meniscus overflow to meniscus overflow within the velocity range of 30 to 200 mm/s for the gap heights investigated. Corresponding data images can be seen in Fig. 4.26. There is a compromise between small gap height and high velocity, as stable flow at a given velocity is maintained at greater gap heights. This is consistent with the critical velocity predicted by Eq. (4.1).

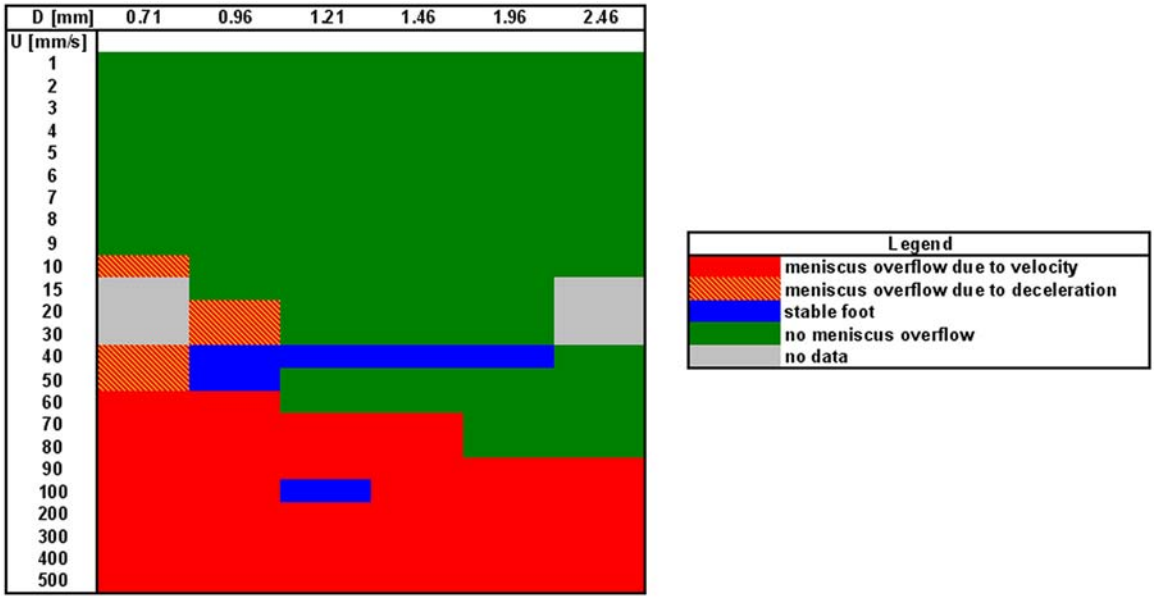

Figure 4.24: Experimentally-determined meniscus overflow map showing gap height versus velocity for Rain-X-treated glass. [Rodríguez, 2004]

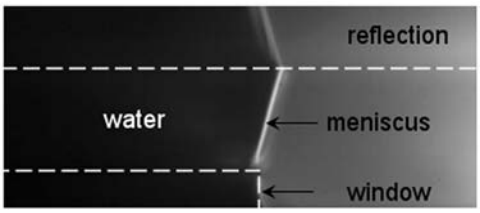

Figure 4.25: Sample image illustrating the "no meniscus overflow" condition on Rain-X-treated glass.

4.3.2 Quartz Substrate

Data images were acquired at various velocities and gap heights with a quartz substrate. The substrate velocity was varied from 1-800 mm/s while the gap height was varied from 0.25 to 2.0 mm. Results depicting the qualitative behavior can be seen in Fig. 4.27. The transition to film pulling occurs abruptly at a velocity of 20-30 mm/s, and appears to be less dependent on gap height than on velocity; this is consistent with the critical velocity for film pulling predicted by Eq. (4.9). The data images corresponding with velocity range of 10 to 200 mm/s, which brackets the transition from film pulling to meniscus overflow,

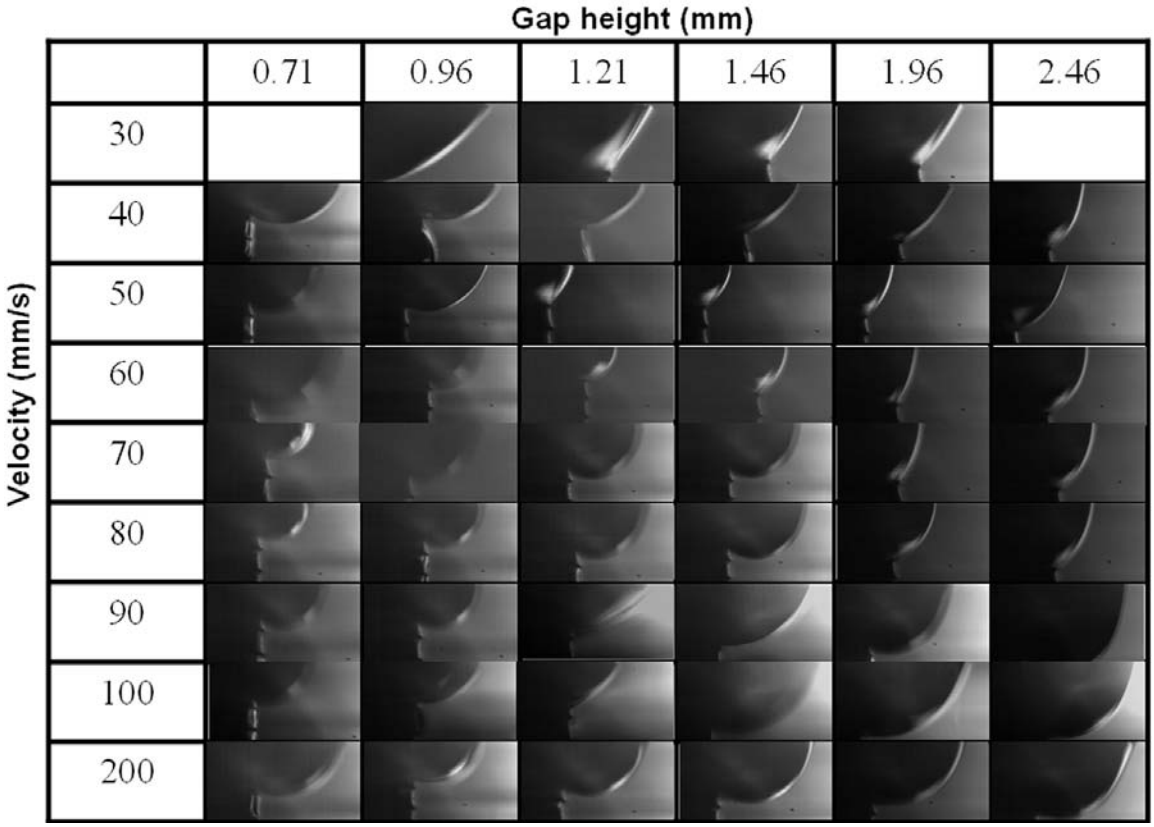

Figure 4.26: Images of the meniscus behavior on Rain-X-treated glass at various gap heights and velocities bracketing the transition from no meniscus overflow to meniscus overflow. [Rodríguez, 2004]

can be seen in Fig. 4.28. In the region exhibiting no meniscus overflow, for a given velocity the meniscus radius of curvature increases and the overall meniscus slope decreases with increasing gap height. This agrees with theory presented earlier, which predicts decreased radius of curvature to compensate for increased viscous pressures at higher velocities. For a given gap height, the meniscus slope becomes more horizontal with increasing velocity. The increasing velocity "pulls" the fluid out further, flattening the meniscus slope. The meniscus tends to be concave in shape when between two hydrophilic surfaces. Only at high velocities and gap heights is the concavity reversed and bulging observed.

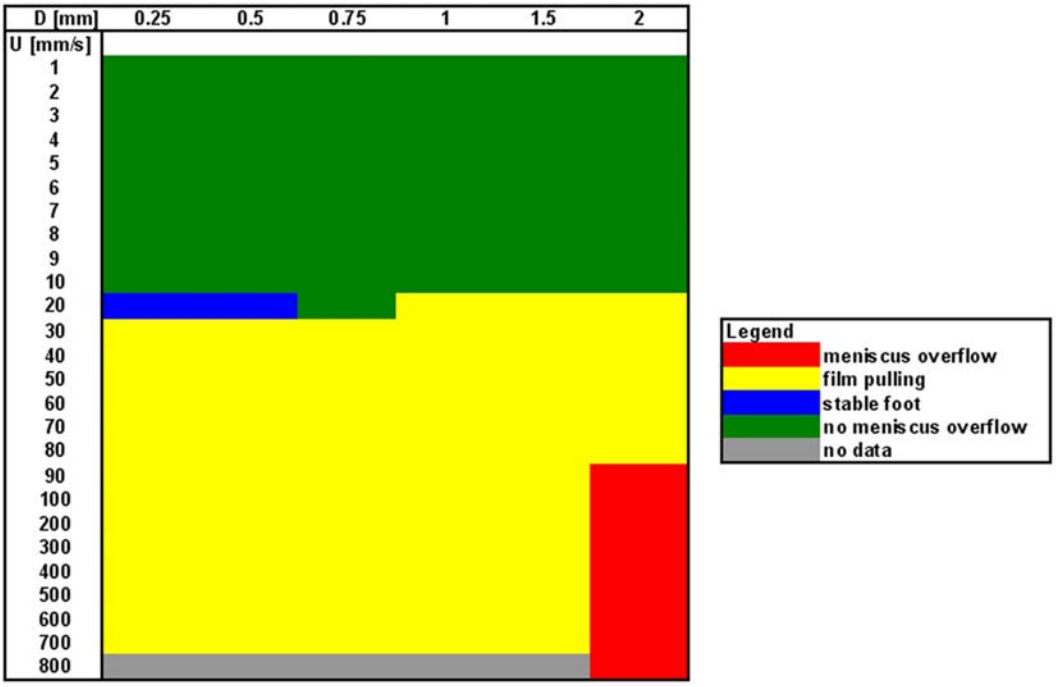

Figure 4.27: Experimentally-determined meniscus overflow map for a quartz substrate.

4.3.3 Comparison with Engineering Model

The critical velocity results on Rain-X-treated glass (data points illustrated in Fig. 4.29) were plotted together with the engineering model predictions in Fig. 4.30. The engineering model was run with an advancing angle of 103.4° and a receding angle of 92.2° on both the substrate and window surfaces. The model predicts greater critical velocities than those observed experimentally; however, model predictions including 0.1 m/s^2 acceleration approach experimental results. This suggests that acceleration effects may have played a significant role in the experiment. Other possible contributing factors are discussed in Sec. 4.3.5.

4.3.4 Acceleration/Deceleration Effects

A high rate of acceleration or deceleration leads to an augmentation of the pressure gradient, which can lead to bulk fluid loss even when the steady state behavior is film pulling or a

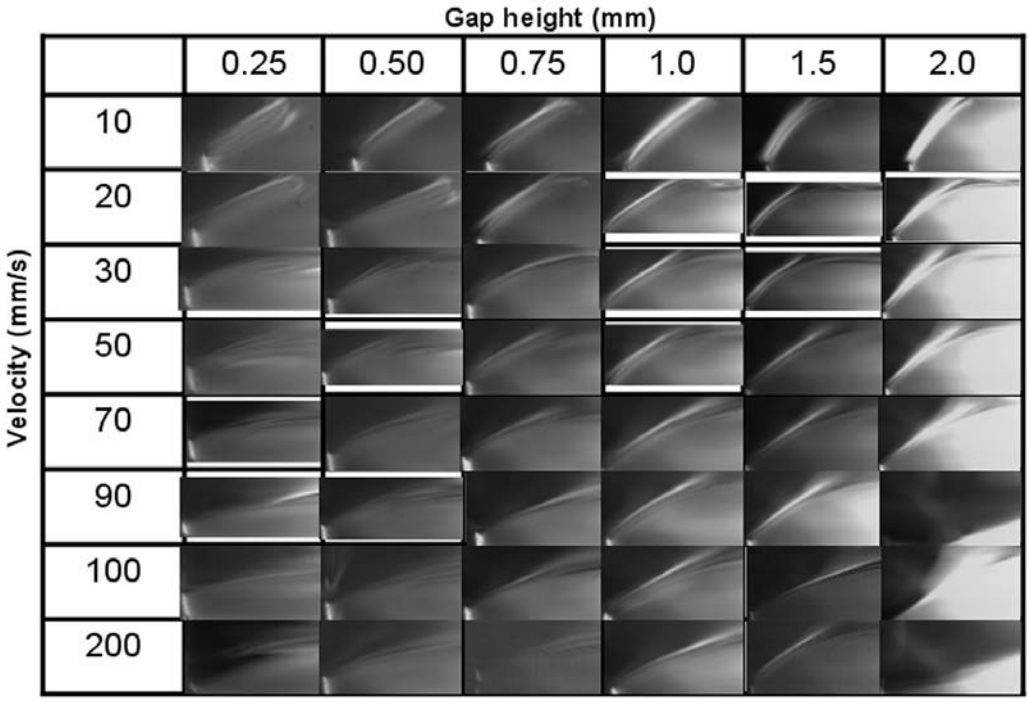

Figure 4.28: Images of the meniscus behavior on a quartz substrate at various gap heights and velocities.

stable "foot". As the substrate decelerates, a bulb of fluid will accumulate at the contact line. An example image of deceleration overflow on a quartz substrate is shown in Fig. 4.31. Deceleration overflow was only observed on the quartz substrate.

Acceleration can lead to a bulge that either stabilizes into a no overflow condition or leads to meniscus overflow. An example image of an acceleration bulge that resulted in acceleration-driven overflow is shown in Fig. 4.32. Acceleration overflow was observed on both Rain-X-treated glass and quartz substrates.

Maps of observed acceleration and deceleration effects are shown in Table 4.1 for the quartz substrate and Table 4.2 for the Rain-X-treated glass. On the quartz surface, larger gap heights appear to increase the occurrence of this behavior. Acceleration overflow on the Rain-X-treated glass occurs at small gap heights. There is no clear trend with velocity on either substrate. The previously presented meniscus overflow conditions were velocity-driven

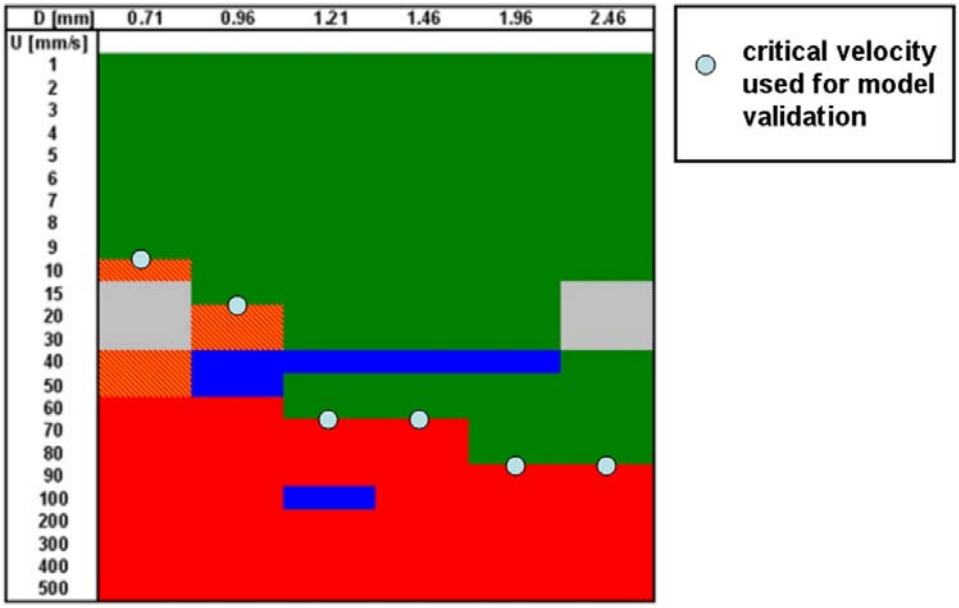

Figure 4.29: Graphical illustration of experimentally-determined critical velocities on Rain-X-treated glass used for comparison with engineering model.

(see Sections 4.3.1 and 4.3.2). However, in some cases it is difficult to distinguish between fluid loss due to accleration/deceleration and steady-state bulk fluid loss due to velocity.

Table 4.1: Acceleration and deceleration overflow observations (AO and DO, respectively) on quartz substrate.

gap [mm]	0.5	0.75	1	1.5	2
V [mm/s]					
60				DO	AO
70				DO	AO
80		DO		AO	
90			DO	AO, DO	AO
100		DO	DO	DO	
200			DO	AO, DO	
300			DO		

4.3.5 Uncontrolled Variables

Several uncontrolled experimental variables may have contributed to variability in the results. This experimental setup provides little control over the initial fill condition. The initial liquid volume can vary from one run to the next, since the gap is filled manually. Higher puddle

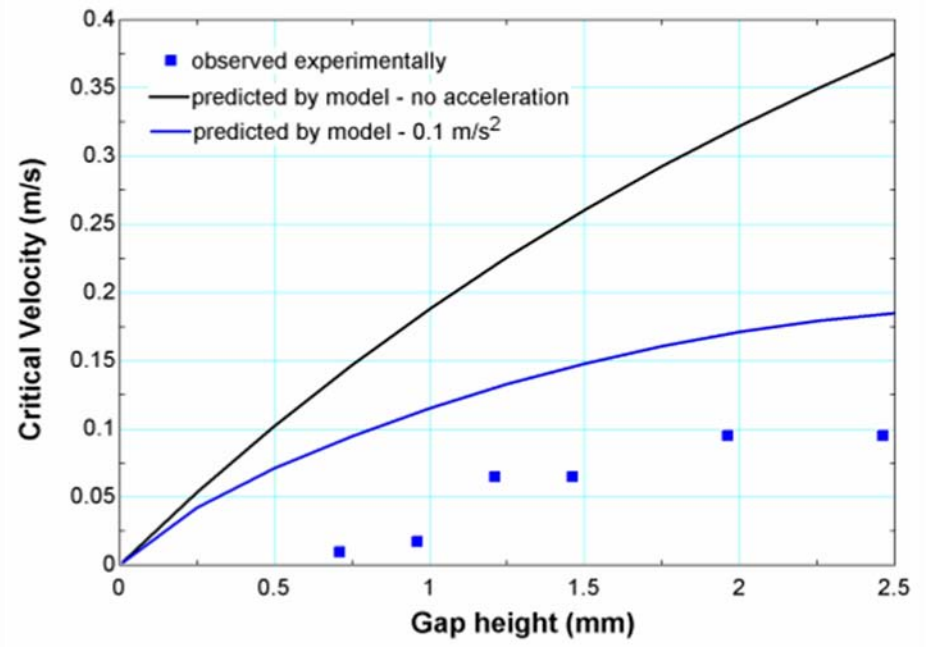

Figure 4.30: Critical velocity for meniscus overflow as a function of gap height, measured and predicted.

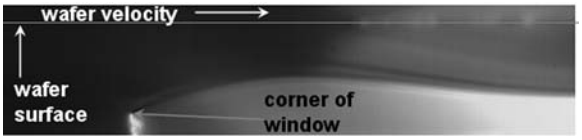

Figure 4.31: Deceleration overflow at 90 mm/s with a 0.75 mm gap on a quartz substrate.

volumes would lead to meniscus overflow at lower velocities and gap heights. The initial shape of the meniscus when substrate motion commences is not controlled. That is, the substrate could have been moving in either direction just prior to a data run. The possible effect of this has not been quantified. Although care was taken to be sure that the meniscus was pinned at the edge of the lens at the start of each duty cycle, since the fill operation is performed manually, it is uncertain that this was always the case. Care was also taken to dry the lens edge after a meniscus overflow episode; however, any remaining water on that surface would encourage bulk meniscus overflow on a subsequent run. The substrate cleanliness is also critical, as particles on the surface can lead to premature film pulling or

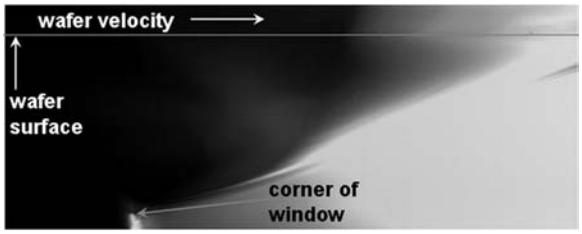

Figure 4.32: Bulge leading to acceleration overflow at 70 mm/s with a 2.0 mm gap on a quartz substrate.

Table 4.2: Acceleration overflow (AO) observations on Rain-X-treated glass.

gap [mm]	0.25	0.5	0.75	1	1.5	2
V [mm/s]						
10	AO					
15						
20		AO				
30		AO				
40	AO					
50	AO					
100		AO	AO	AO	AO	AO

fluid loss.

4.4 Conclusions

For the anticipated flow conditions and surface characteristics in immersion lithography, fluid deposition on the wafer surface is expected based on the experimental and modeling results described above. Meniscus overflow and thin film pulling are the two principal mechanisms observed and both lead to fluid deposition on the surface. Thick film pulling is an additional mechanism that has been observed but is not well-understood. An engineering model has been developed and verified under a limited set of conditions; this tool can be applied to map critical velocity for bulk meniscus overflow and film pulling for various potential shower head designs. The engineering model can be used to by tool designers to ensure that fluid deposition on the wafer surface is avoided.

Chapter 5

Summary

A series of investigations were conducted to examine the effect of surface characteristics on contact line behavior in immersion lithography, a potential next-generation lithography technology. Behaviors that could lead to manufacturing problems were examined experimentally and, where possible, the results were compared to CFD simulations.

Static contact angle and hysteresis measurements were used to characterize six photoresist-coated wafer surfaces and three baseline surfaces. Resist-coated wafers exhibit a high degree of surface heterogeneity; some resist-coated wafers exhibit distinct contact angles in different locations on the surface. The measured angles provided input into CFD models. Dynamic contact angles were measured on all test surfaces for velocities relevant to immersion lithography. Dynamic contact angles tend to increase with increasing velocity. For the conditions tested, the advancing dynamic contact angle does not reach 180°, which would result in air entrainment.

Two potential air entrainment mechanisms were investigated. A numerical and experimental study of air entrainment due to flow over topography was conducted. Air entrainment was neither predicted nor observed due to flow over topography. An experimental study was conducted in which a droplet on the substrate surface was forced into the meniscus. Air was entrained in the immersion fluid due to droplet impact on Rain-X-treated glass and quartz surfaces (which have properties bounding those of resist-coated wafers) at velocities and gap heights expected in immersion lithography.

The receding meniscus behavior was characterized; film pulling and meniscus overflow

are two failure mechanisms of the receding meniscus. Both lead to droplet deposition on the substrate surface. An engineering model was developed that is capable of approximately predicting the conditions that lead to meniscus overflow. Meniscus overflow and film pulling maps were observed experimentally at velocities and gap heights consistent with those expected in immersion lithography on both Rain-X-treated glass and quartz surfaces. There is a compromise between small gap height and high velocity, as stable flow at a given velocity is maintained at greater gap heights. Acceleration and deceleration effects are both predicted and observed to be significant contributors to meniscus overflow. Decreasing the gap height results in an increase in the acceleration-induced pressure gradient because the increased viscous force tends to more strongly link the fluid motion to the wafer motion. Design of immersion lithography systems must include measures to avoid these problems.

Bibliography

P.-G. de Gennes, F. Brochard-Wyard, and D. Quéré. *Capillarity and Wetting Phenomena*. Springer, New York, New York, USA, 2004.

K. Derbyshire. Optical lithography's liquid future. *Semiconductor Manufacturing*, 5(3): 18–30, 2004.

Y. Fan, N. Lafferty, A. Bourov, L. Zavyalova, and B. W. Smith. Study of air bubble induced light scattering effect on image quality in 193 nm immersion lithography. *Proceedings of SPIE - The International Society for Optical Engineering, Optical Microlithography XVII*, 5377(PART 1):47–486, 2004.

D. Gil, T.A. Brunner, C. Fonseca, N. Seong, R. Streefkerk, C. Wagner, and M. Stavenga. Immersion lithography: New opportunities for semiconductor manufacturing. To appear in *Journal of Vacuum Science and Technology B*, 2004.

ICKnowledge, LLC. Technology backgrounder: Immersion lithography. Internet (http://www.icknowledge.com/misc_technology/Immersion Lithography.pdf), 2003.

R. E. Jr. Johnson and R. H. Dettre. Wetting of low-energy surfaces. In J. C. Berg, editor, *Wettability*. Marcel Dekker, Inc., New York, New York, U.S.A., 1993.

Nikon Corporation. Development of ArF immersion stepper for mass-production applications. Internet, February 2004.

J. G. Petrov, R. V. Sedev, and P. G. Petrov. Effect of geometry on steady wetting kinetics and critical velocity of film entrainment. *Advances in Colloid and Interface Science*, 38: 229–269, 1992.

D. Rodríguez. Personal communication. University of Wisconsin-Madison, 2004.

Semiconductor Consulting Services, Inc. Basic photolithography process. Internet (http://www.semiconsulting.com/dl/10370a.pdf), March 2001.

T. A. Shedd. A general model for estimating bubble dissolution and droplet evaporation times. Submitted to *Journal of Microlithography, Microfabrication and Microsystems*, 2005.

M. Switkes, T. M. Bloomstein, R. R. Kunz, M. Rothchild, and T. A. Shedd. Resist behavior in liquid immersion lithography. To appear in *Journal of Vacuum Science and Technology B*, 2004.

M. Switkes and M. Rothschild. Resolution enhancement of 157 nm lithography by liquid immersion. *Journal of Microlithography, Microfabrication, and Microsystems*, 1(3):225–228, 2002.

A. Wei, A. Abdo, G. F. Nellis, R. L. Engelstad, and E. G. Lovell. Predicting air entrainment due to topography during filling and scanning process for immersion lithography. To appear in *Journal of Vacuum Science and Technology B*, 2004.

A. C. Wei. Thermofluid simulations for immersion lithography. Master's thesis, University of Wisconsin-Madison, Madison, WI, 2004.

Appendix

Data for Fig. 2.17:

Table 5.1: Dynamic contact angle data at various gap heights on quartz substrate at three velocities.

	Gap Height (mm)					
	0.25	0.5	0.75	1	1.5	2
Angle at 0.01 m/s	**79.1**	**73.2**	**71.0**	**74.1**	**68.5**	**67.7**
stdev	7.14	4.44	4.24	3.31	5.40	4.21
count	52	99	94	47	93	100
95% conf.	1.94	0.87	0.86	0.95	1.10	0.83
Angle at 0.05 m/s	**95.8**	**99.6**	**98.5**	**99.2**	**85.0**	**83.3**
stdev	2.93	3.86	4.05	3.75	4.06	5.24
count	98	99	97	88	99	59
95 % conf.	0.58	0.76	0.81	0.78	0.80	1.34
Angle at 0.1 m/s	**101.5**	**98.6**	**102.3**	**100.4**	**87.7**	**102.2**
stdev	6.67	8.27	6.68	5.32	8.27	4.41
count	58	98	70	86	58	51
95% conf.	1.72	1.64	1.56	1.12	2.13	1.21

Data for Fig. 2.18:

Table 5.2: Dynamic contact angle data on Rain-X-treated glass and quartz surfaces.

	RainX		Quartz	
Velocity (m/s)	Angle (actual)	95% Confidence Interval	Angle (actual)	95% Confidence Interval
0.01	110.9	0.58	72.9	1.60
0.02	113.1	0.54	80.2	1.09
0.03	113.0	0.60	85.7	2.90
0.04	114.2	0.50	109.0	3.30
0.05	113.5	0.89	108.8	1.21
0.06	115.9	1.00	116.1	1.44
0.07	117.4	0.77	123.7	1.99
0.08	116.7	0.64	115.1	1.36
0.09	115.7	0.80	116.7	2.50
0.1	116.7	0.59	115.2	1.17
0.2	117.3	0.77	117.4	1.63
0.3	116.6	1.14	120.7	1.62
0.4	114.4	1.51		1.62
0.5	117.3	0.88		
0.6	117.1	0.90		
0.7	118.3	1.03		
0.8	119.5	0.93		
0.9	119.1	1.88		
1	119.0	1.97		

Data for Figures 2.19 and 2.20:

Table 5.3: Dynamic contact angle data photoresist-coated wafer surfaces.

	ARCH GAR8105		JSR 237J		TOK TARF6111		Sumitomo PAR817		TOK TARF7047		TOK TSP-3A	
Velocity (m/s)	Angle (Actual)	95% Confidence Interval	Angle (Actual)	95% Confidence Interval	Angle (Actual)	95% Confidence Interval	Angle (Actual)	95% Confidence Interval	Angle (Actual)	95% Confidence Interval	Angle (Actual)	95% Confidence Interval
0.01	94.58	0.50	89.8	1.03	99.3	0.87	101.5	1.06	89.7	0.47	128.0	0.28
0.02	95.0	0.53	90.4	1.00	105.1	1.51	105.1	0.65	95.3	0.72	129.3	0.29
0.03	93.6	0.43	91.9	0.83	107.9	1.32	106.2	0.71	96.0	0.84	129.5	0.35
0.04	92.5	0.59	93.0	0.78	110.1	1.29	103.8	0.38	95.9	0.93	129.9	0.51
0.05	90.8	0.49	91.3	0.77	110.1	1.17	107.7	1.04	95.5	0.67	132.3	0.33
0.06	92.5	0.79	93.2	0.84	110.6	0.77	108.1	1.15	95.9	0.83	129.2	0.37
0.07	91.2	0.58	94.1	0.92	111.7	1.39	110.7	1.14	94.6	0.77	128.7	0.39
0.08	91.9	1.05	93.1	0.97	111.7	1.43	108.7	1.21	95.9	0.78	130.7	0.57
0.09	90.2	0.49	93.3	0.60	110.7	1.36	112.7	1.41	97.8	1.01	131.0	0.44
0.10	90.2	0.91	97.3	0.76	110.3	1.32	113.6	0.71	100.8	1.22	130.2	0.47
0.20	90.7	0.62	95.1	0.58	121.4	3.11	115.8	1.09	102.5	0.43	132.5	0.41
0.30	91.9	0.92	101.7	2.62	129.2	1.75	122.4	1.53	98.8	1.45	133.8	0.61
0.40	92.8	0.91	101.6	3.48	126.6	1.60	125.2	1.12	108.0	1.96	134.2	0.44
0.50	93.9	1.21			109.8	3.74	118.8	1.49	101.9	2.06	130.6	0.86
0.60	92.6	1.68					128.7	2.04	104.4	2.21		
0.70	94.4	1.57					115.6	1.73	102.0	1.81		
0.80	92.5	2.65					126.6	0.78	106.7	1.33		
0.90	93.7	1.56					122.9	1.36	101.1	1.07		
1.00	85.9	3.07					119.8	1.85	102.8	1.43		